Adaptive High-Order A-WENO Schemes Based on a New Local Smoothness Indicator

Alina Chertock[1], Shaoshuai Chu[2] and Alexander Kurganov[2,3,*]

[1]*Department of Mathematics, North Carolina State University, Raleigh, NC 27695, USA.*

[2]*Department of Mathematics, Southern University of Science and Technology, Shenzhen 518055, China.*

[3]*Shenzhen International Center for Mathematics and Guangdong Provincial Key Laboratory of Computational Science and Material Design, Southern University of Science and Technology, Shenzhen 518055, China.*

Dedicated to Professor Tao Tang on the occasion of his 60th birthday.

Abstract. We develop new adaptive alternative weighted essentially non-oscillatory (A-WENO) schemes for hyperbolic systems of conservation laws. The new schemes employ the recently proposed local characteristic decomposition based central-upwind numerical fluxes, the three-stage third-order strong stability preserving Runge-Kutta time integrator, and the fifth-order WENO-Z interpolation. The adaptive strategy is implemented by applying the limited interpolation only in the parts of the computational domain where the solution is identified as rough with the help of a smoothness indicator. We develop and use a new simple and robust local smoothness indicator (LSI), which is applied to the solutions computed at each of the three stages of the ODE solver. The new LSI and adaptive A-WENO schemes are tested on the Euler equations of gas dynamics. We implement the proposed LSI using the pressure, which remains smooth at contact discontinuities, while our goal is to detect other rough areas and apply the limited interpolation mostly in the neighborhoods of the shock waves. We demonstrate that the new adaptive schemes are highly accurate, non-oscillatory, and robust. They outperform their fully limited counterparts (the A-WENO schemes with the same numerical fluxes and ODE solver but with the WENO-Z interpolation employed everywhere) while being less computationally expensive.

Corresponding author. Email addresses: `chertock@math.ncsu.edu` (A. Chertock), `chuss2019@mail.sustech.edu.cn` (S. Chu), `alexander@sustech.edu.cn` (A. Kurganov)

1. Introduction

This paper focuses on developing high-order finite-difference methods for hyperbolic systems of conservation laws. We consider one-dimensional (1-D),

$$U_t + F(U)_x = 0, \tag{1.1}$$

and two-dimensional (2-D),

$$U_t + F(U)_x + G(U)_y = 0, \tag{1.2}$$

systems, though the proposed techniques can be directly extended to higher-dimensional cases. Here, x and y are spatial variables, t is the time, $U \in \mathbb{R}^d$ is a vector of unknown functions, and $F : \mathbb{R}^d \to \mathbb{R}^d$ and $G : \mathbb{R}^d \to \mathbb{R}^d$ are nonlinear fluxes.

It is well-known that solutions of (1.2) may develop complicated wave structures, including shocks, rarefactions, and contact discontinuities, even when the initial data are infinitely smooth. Therefore, it is challenging to develop highly accurate and robust numerical methods for (1.2). We refer the reader to various existing numerical methods, including high-order ones, e.g., the monographs and review papers [8, 30, 35, 40, 55, 56, 60] and references therein.

Semi-discretization of (1.1) and (1.2) offers one of the popular frameworks for constructing high-order finite-volume and finite-difference schemes: the spatial derivatives are approximated using appropriate numerical fluxes. At the same time, the time evolution is conducted with the help of a high-order and stable ODE solver. To achieve a high order of spatial accuracy, the numerical fluxes must be evaluated using the point values of U obtained by an appropriate piecewise polynomial reconstruction (interpolation) of the computed solution. In order to enforce nonlinear stability, the reconstructions have to employ nonlinear limiters designed to prevent spurious oscillations in the nonsmooth parts of the solutions. Popular finite-volume reconstructions, such as essentially non-oscillatory (ENO) (see, e.g., [1, 28, 29, 56]) and weighted ENO (WENO) (see, e.g., [6, 31, 44, 55, 56]) ones are highly accurate, but typically finite-volume ENO and WENO schemes are computationally expensive, especially in the multidimensional case. More efficient implementations of ENO and WENO reconstructions can be carried out within the finite-difference framework in a dimension-by-dimension manner; see, e.g., [7, 11, 12, 31, 57, 58]. Unfortunately, the finite-difference schemes, which are directly based on finite-volume reconstructions, rely on flux splittings, substantially increasing the amount of numerical diffusion present in finite-volume ENO and WENO schemes. This drawback of finite-difference WENO schemes was overcome in [32] (also see [43]), where alternative WENO (A-WENO) schemes were introduced. A-WENO schemes employ standard finite-volume numerical fluxes (without any need for flux splitting and related modifications), whose accuracy, in the context of finite-difference schemes, is limited to the second order, while a high order is achieved using the flux Taylor expansion and high-order WENO-Z interpolations, which were developed in [16, 21, 32, 43, 64]. For several recent A-WENO schemes based on different finite-volume numerical fluxes, we refer the reader to [62–64].

Even though WENO-Z interpolations are relatively computationally inexpensive and can be applied in a dimension-by-dimension manner, the computational cost can be further reduced by avoiding the use of any nonlinear limiters in the smooth parts of the solution as it was done in the context of hybrid WENO schemes; see, e.g., [14, 41, 46]. In general, in order to derive a robust scheme adaption technique, one needs to detect nonsmooth parts of the solution efficiently. This can be done in many ways using various existing smoothness indicators. In [2, 46], a very simple indicator based on undivided differences was introduced. In [9, 10], discontinuities were detected using Richardson-type estimates of the local truncation error of the solution. A total variation based troubled-cell indicator was developed in [50, 66]. A more heuristic approach is examined in [47, 51], where the local wave strengths of the upwind scheme were used as a measure of solution smoothness. In [3–5, 14], multiresolution coefficients of wavelets expansions were used. In [22, 23], the edges in the computed solution were detected using its Fourier coefficient. One can also identify the rough parts of the computed solution using the numerical production of entropy (see, e.g., [48, 49]), the entropy residual (see, e.g., [26, 27]), or the weak local residual (see, e.g., [15, 33, 34]).

In this paper, we develop a new, very simple, and robust local smoothness indicator based on the Taylor expansion in time, applied to the computed solutions obtained at each stage of the three-stage third-order strong stability preserving (SSP) Runge-Kutta solver; see, e.g., [24, 25]. We first demonstrate that the proposed LSI can accurately detect smooth and nonsmooth solution regions. We then apply the new LSI to design the following scheme adaption strategy in the context of the A-WENO schemes: we use the fifth-order nonlinear WENO-Z interpolation in the detected rough parts of the computed solutions while employing a nonlimited fifth-order interpolants in smooth areas.

The developed scheme adaption strategy is implemented using the recently proposed local characteristic decomposition based central-upwind numerical flux from [13] and applied to both the 1-D and 2-D Euler equations of gas dynamics, for which we design the LSI based on the pressure rather than on the density or any other conservative variable. This choice is motivated by the results obtained in [15], where it has been demonstrated that applying a nonlinear stabilization mechanism is crucial for the shock areas while isolated linearly degenerate contact waves can be accurately captured using the nonlimited high-order reconstruction. We test the resulting adaptive fifth-order A-WENO scheme on several numerical examples and demonstrate that it outperforms the corresponding fifth-order A-WENO the scheme, which is implemented without the proposed adaptation, that is, employs the WENO-Z interpolation throughout the entire computational domain.

The paper is organized as follows. In Section 2, we briefly describe the proposed 1-D and 2-D fifth-order A-WENO schemes. In Section 3, we introduce the new LSI and then illustrate its performance on the Sod shock-tube problem for the 1-D Euler equations of gas dynamics. In Section 4, we describe 1-D and 2-D scheme adaption strategies based on the proposed LSI. In Section 5, we present a number of the 1-D and 2-D numerical results to demonstrate the performance of the proposed adaptive A-WENO schemes and compare it with the fully limited A-WENO schemes. Finally, in Section 6, we give concluding remarks.

2. Fifth-Order A-WENO Schemes

In this section, we describe the fifth-order finite-difference A-WENO schemes introduced in [32] (see also [43, 62–64]).

2.1. 1-D A-WENO schemes

We first consider the 1-D system (1.1) and introduce uniform cells $C_j := [x_{j-1/2}, x_{j+1/2}]$ of size $x_{j+1/2} - x_{j-1/2} \equiv \Delta x$ centered at $x_j = (x_{j-1/2} + x_{j+1/2})/2$ for $j = 1, \ldots, N_x$, so that the computational domain is $[x_{1/2}, x_{N_x+1/2}]$. We suppose that at a certain time $t \geq 0$, the point values of the computed solution, $U_j(t)$, are available, and in what follows, we will suppress the time-dependence of all of the indexed quantities for the sake of brevity.

Following [32], U_j are evolved in time by numerically solving the following system of ODEs:

$$\frac{\mathrm{d}U_j}{\mathrm{d}t} = -\frac{\mathscr{F}_{j+1/2} - \mathscr{F}_{j-1/2}}{\Delta x}, \tag{2.1}$$

where $\mathscr{F}_{j+1/2}$ is the fifth-order accurate numerical flux defined by

$$\mathscr{F}_{j+1/2}\big(U^-_{j+1/2}, U^+_{j+1/2}\big) = \mathscr{F}^{\mathrm{FV}}_{j+1/2}\big(U^-_{j+1/2}, U^+_{j+1/2}\big) - \frac{1}{24}(\Delta x)^2 (F_{xx})_{j+1/2}$$
$$+ \frac{7}{5760}(\Delta x)^4 (F_{xxxx})_{j+1/2}. \tag{2.2}$$

Here, $\mathscr{F}^{\mathrm{FV}}_{j+1/2}$ is a finite-volume numerical flux, and $(F_{xx})_{j+1/2}$ and $(F_{xxxx})_{j+1/2}$ are the higher-order correction terms computed by the fourth- and second-order accurate finite differences, respectively

$$(F_{xx})_{j+1/2} = \frac{1}{48(\Delta x)^2}\Big[-5F_{j-2} + 39F_{j-1} - 34F_j - 34F_{j+1} + 39F_{j+2} - 5F_{j+3}\Big],$$
$$(F_{xxxx})_{j+1/2} = \frac{1}{2(\Delta x)^4}\Big[F_{j-2} - 3F_{j-1} + 2F_j + 2F_{j+1} - 3F_{j+2} + F_{j+3}\Big],$$

where $F_j := F(U_j)$.

In the numerical experiments reported in Section 5.1, we have used a recently proposed local characteristics decomposition (LCD) based central-upwind (CU) numerical flux from [13], which reads as

$$\mathscr{F}^{\mathrm{FV}}_{j+1/2}\big(U^-_{j+1/2}, U^+_{j+1/2}\big) = \frac{F_j + F_{j+1}}{2} + D_{j+1/2}\big(U^-_{j+1/2}, U^+_{j+1/2}\big), \tag{2.3}$$

where $D_{j+1/2}$ is the following numerical diffusion term:

$$D_{j+1/2}\big(U^-_{j+1/2}, U^+_{j+1/2}\big) = R_{j+1/2}P_{j+1/2}R^{-1}_{j+1/2}\left[F\big(U^-_{j+1/2}\big) - \frac{F_j + F_{j+1}}{2}\right]$$
$$+ R_{j+1/2}M_{j+1/2}R^{-1}_{j+1/2}\left[F\big(U^+_{j+1/2}\big) - \frac{F_j + F_{j+1}}{2}\right]$$
$$+ R_{j+1/2}Q_{j+1/2}R^{-1}_{j+1/2}\big(U^+_{j+1/2} - U^-_{j+1/2}\big). \tag{2.4}$$

Here, $R_{j+1/2}$ is the matrix used for the LCD in the neighborhood of $x = x_{j+1/2}$ (see Appendix B),

$$P_{j+1/2} = \mathrm{diag}\big((P_1)_{j+1/2},\ldots,(P_d)_{j+1/2}\big),$$
$$M_{j+1/2} = \mathrm{diag}\big((M_1)_{j+1/2},\ldots,(M_d)_{j+1/2}\big),$$
$$Q_{j+1/2} = \mathrm{diag}\big((Q_1)_{j+1/2},\ldots,(Q_d)_{j+1/2}\big)$$

with

$$
\begin{aligned}
&\big((P_i)_{j+1/2},(M_i)_{j+1/2},(Q_i)_{j+1/2}\big)\\
&= \begin{cases} \dfrac{1}{\Delta\lambda_{j+1/2}}\big((\lambda_i^+)_{j+1/2},-(\lambda_i^-)_{j+1/2},(\lambda_i^+)_{j+1/2}(\lambda_i^-)_{j+1/2}\big), & \text{if}\quad \Delta\lambda_{j+1/2} > \varepsilon,\\ 0, & \text{otherwise,} \end{cases}
\end{aligned}
$$

where $\Delta\lambda_{j+1/2} := (\lambda_i^+)_{j+1/2} - (\lambda_i^-)_{j+1/2}$. The one-sided local characteristic speeds,

$$
\begin{aligned}
(\lambda_i^+)_{j+1/2} &= \max\left\{\lambda_i\big(A(U_{j+1/2}^-)\big),\ \lambda_i\big(A(U_{j+1/2}^+)\big),\ 0\right\},\\
(\lambda_i^-)_{j+1/2} &= \min\left\{\lambda_i\big(A(U_{j+1/2}^-)\big),\ \lambda_i\big(A(U_{j+1/2}^+)\big),\ 0\right\},
\end{aligned}
\qquad i = 1,\ldots,d \qquad (2.5)
$$

are computed using the eigenvalues $\lambda_1(A) \le \cdots \le \lambda_d(A)$ of the Jacobian $A = \partial F/\partial U$, and ε is a very small desingularization constant, taken $\varepsilon = 10^{-10}$ in all of the numerical examples reported in Section 5.

In (2.3)-(2.5), $U_{j+1/2}^\pm$ are the right/left-sided values of U at the cell interface $x = x_{j+1/2}$. In order to ensure the desired fifth order of accuracy, one needs to use a fifth order accurate approximation of the point values $U_{j+1/2}^\pm$. It is also important to guarantee that the resulting scheme is (essentially) non-oscillatory. This can be done by implementing a certain nonlinear limiting procedure like the fifth-order WENO-Z interpolation from [16, 21, 32, 43, 64] (see Appendix A) applied to the local characteristic variables (see Appendix B), or a certain adaption strategy like the one we will introduce in Section 4.

2.2. 2-D A-WENO schemes

We now turn our attention to the 2-D system (1.2) and describe 2-D fifth-order A-WENO schemes.

We consider a rectangular computational domain $[x_{1/2}, x_{N_x+1/2}]\times[y_{1/2}, y_{N_y+1/2}]$, which is covered with uniform cells $C_{j,k} := [x_{j-1/2}, x_{j+1/2}]\times[y_{k-1/2}, y_{k+1/2}]$ centered at $(x_j, y_k) = ((x_{j-1/2}+x_{j+1/2})/2, (y_{k-1/2}+y_{k+1/2})/2)$ with $x_{j+1/2}-x_{j-1/2} \equiv \Delta x$ and $y_{k+1/2}-y_{k-1/2} \equiv \Delta y$ for $j = 1,\ldots,N_x$ and $k = 1,\ldots,N_y$. We also assume that the computed point values $U_{j,k} \approx U(x_j, y_k, t)$ are available at a certain time level t. We then evolve $U_{j,k}$ in time by numerically solving the following system of ODEs:

$$\frac{\mathrm{d}U_{j,k}}{\mathrm{d}t} = -\frac{\mathscr{F}_{j+1/2,k} - \mathscr{F}_{j-1/2,k}}{\Delta x} - \frac{\mathscr{G}_{j,k+1/2} - \mathscr{G}_{j,k-1/2}}{\Delta y}, \qquad (2.6)$$

where $\mathscr{F}_{j+1/2,k}$ and $\mathscr{G}_{j,k+1/2}$ are the fifth-order accurate numerical fluxes defined by

$$\mathscr{F}_{j+1/2,k} = \mathscr{F}^{\mathrm{FV}}_{j+1/2,k}\big(U^{\mathrm{E}}_{j,k}, U^{\mathrm{W}}_{j+1,k}\big) - \frac{1}{24}(\Delta x)^2 (F_{xx})_{j+1/2,k}$$
$$+ \frac{7}{5760}(\Delta x)^4 (F_{xxxx})_{j+1/2,k}, \tag{2.7a}$$

$$\mathscr{G}_{j,k+1/2} = \mathscr{G}^{\mathrm{FV}}_{j,k+1/2}\big(U^{\mathrm{N}}_{j,k}, U^{\mathrm{S}}_{j,k+1}\big) - \frac{1}{24}(\Delta y)^2 (G_{yy})_{j,k+1/2}$$
$$+ \frac{7}{5760}(\Delta y)^4 (G_{yyyy})_{j,k+1/2}. \tag{2.7b}$$

Here, $\mathscr{F}^{\mathrm{FV}}_{j+1/2,k}$ and $\mathscr{G}^{\mathrm{FV}}_{j,k+1/2}$ are finite-volume fluxes, whereas $(F_{xx})_{j+1/2,k}$, $(G_{yy})_{j,k+1/2}$, $(F_{xxxx})_{j+1/2,k}$, and $(G_{yyyy})_{j,k+1/2}$ are the higher-order correction terms computed by the fourth- and second-order accurate finite differences, respectively

$$(F_{xx})_{j+1/2,k} = \frac{1}{48(\Delta x)^2}\big(-5F_{j-2,k} + 39F_{j-1,k} - 34F_{j,k} - 34F_{j+1,k} + 39F_{j+2,k} - 5F_{j+3,k}\big),$$

$$(F_{xxxx})_{j+1/2,k} = \frac{1}{2(\Delta x)^4}\big(F_{j-2,k} - 3F_{j-1,k} + 2F_{j,k} + 2F_{j+1,k} - 3F_{j+2,k} + F_{j+3,k}\big),$$

$$(G_{yy})_{j,k+1/2} = \frac{1}{48(\Delta y)^2}\big(-5G_{j,k-2} + 39G_{j,k-1} - 34G_{j,k} - 34G_{j,k+1} + 39G_{j,k+2} - 5G_{j,k+3}\big),$$

$$(G_{yyyy})_{j,k+1/2} = \frac{1}{2(\Delta y)^4}\big(G_{j,k-2} - 3G_{j,k-1} + 2G_{j,k} + 2G_{j,k+1} - 3G_{j,k+2} + G_{j,k+3}\big),$$

where $F_{j,k} := F(U_{j,k})$ and $G_{j,k} := G(U_{j,k})$.

In the numerical experiments reported in Section 5.2, we have used the 2-D LCD-based CU numerical fluxes from [13]

$$\mathscr{F}^{\mathrm{FV}}_{j+1/2,k}\big(U^{\mathrm{E}}_{j,k}, U^{\mathrm{W}}_{j+1,k}\big) = \frac{F_{j,k} + F_{j+1,k}}{2} + D_{j+1/2,k}\big(U^{\mathrm{E}}_{j,k}, U^{\mathrm{W}}_{j+1,k}\big),$$
$$\mathscr{G}^{\mathrm{FV}}_{j,k+1/2}\big(U^{\mathrm{N}}_{j,k}, U^{\mathrm{S}}_{j,k+1}\big) = \frac{G_{j,k} + G_{j,k+1}}{2} + D_{j,k+1/2}\big(U^{\mathrm{N}}_{j,k}, U^{\mathrm{S}}_{j,k+1}\big),$$
$$\tag{2.8}$$

where $D_{j+1/2,k}$ and $D_{j,k+1/2}$ are numerical diffusion terms defined by

$$D_{j+1/2,k}\big(U^{\mathrm{E}}_{j,k}, U^{\mathrm{W}}_{j+1,k}\big) = R_{j+1/2,k}P_{j+1/2,k}R^{-1}_{j+1/2,k}\left[F\big(U^{\mathrm{E}}_{j,k}\big) - \frac{F_{j,k} + F_{j+1,k}}{2}\right]$$
$$+ R_{j+1/2,k}M_{j+1/2,k}R^{-1}_{j+1/2,k}\left[F\big(U^{\mathrm{W}}_{j+1,k}\big) - \frac{F_{j,k} + F_{j+1,k}}{2}\right]$$
$$+ R_{j+1/2,k}Q_{j+1/2,k}R^{-1}_{j+1/2,k}\big(U^{\mathrm{W}}_{j+1,k} - U^{\mathrm{E}}_{j,k}\big),$$
$$D_{j,k+1/2}\big(U^{\mathrm{N}}_{j,k}, U^{\mathrm{S}}_{j,k+1}\big) = R_{j,k+1/2}P_{j,k+1/2}R^{-1}_{j,k+1/2}\left[G\big(U^{\mathrm{N}}_{j,k}\big) - \frac{G_{j,k} + G_{j,k+1}}{2}\right]$$
$$+ R_{j,k+1/2}M_{j,k+1/2}R^{-1}_{j,k+1/2}\left[G\big(U^{\mathrm{S}}_{j,k+1}\big) - \frac{G_{j,k} + G_{j,k+1}}{2}\right]$$
$$+ R_{j,k+1/2}Q_{j,k+1/2}R^{-1}_{j,k+1/2}\big(U^{\mathrm{S}}_{j,k+1} - U^{\mathrm{N}}_{j,k}\big).$$
$$\tag{2.9}$$

The matrices $R_{j+1/2,k}$ and $R_{j,k+1/2}$ are used for the LCD in the neighborhoods of $(x,y) = (x_{j+1/2}, y_k)$ and $(x,y) = (x_j, y_{k+1/2})$, respectively, and

$$
\begin{aligned}
P_{j+1/2,k} &= \mathrm{diag}\big((P_1)_{j+1/2,k},\dots,(P_d)_{j+1/2,k}\big),\\
P_{j,k+1/2} &= \mathrm{diag}\big((P_1)_{j,k+1/2},\dots,(P_d)_{j,k+1/2}\big),\\
M_{j+1/2,k} &= \mathrm{diag}\big((M_1)_{j+1/2,k},\dots,(M_d)_{j+1/2,k}\big),\\
M_{j,k+1/2} &= \mathrm{diag}\big((M_1)_{j,k+1/2},\dots,(M_d)_{j,k+1/2}\big),\\
Q_{j+1/2,k} &= \mathrm{diag}\big((Q_1)_{j+1/2,k},\dots,(Q_d)_{j+1/2,k}\big),\\
Q_{j,k+1/2} &= \mathrm{diag}\big((Q_1)_{j,k+1/2},\dots,(Q_d)_{j,k+1/2}\big)
\end{aligned}
$$

with

$$
\begin{aligned}
&\big((P_i)_{j+1/2,k},(M_i)_{j+1/2,k},(Q_i)_{j+1/2,k}\big)\\
&= \begin{cases}
\dfrac{1}{\Delta(\lambda_i)_{j+1/2,k}}\big((\lambda_i^+)_{j+1/2,k}, -(\lambda_i^-)_{j+1/2,k}, (\lambda_i^+)_{j+1/2,k}(\lambda_i^-)_{j+1/2,k}\big), & \text{if } \Delta(\lambda_i)_{j+1/2,k} > \varepsilon,\\
0, & \text{otherwise,}
\end{cases}\\
&\big((P_i)_{j,k+1/2},(M_i)_{j,k+1/2},(Q_i)_{j,k+1/2}\big)\\
&= \begin{cases}
\dfrac{1}{\Delta(\mu_i)_{j,k+1/2}}\big((\mu_i^+)_{j,k+1/2}, -(\mu_i^-)_{j,k+1/2}, (\mu_i^+)_{j,k+1/2}(\mu_i^-)_{j,k+1/2}\big), & \text{if } \Delta(\mu_i)_{j,k+1/2} > \varepsilon,\\
0, & \text{otherwise.}
\end{cases}
\end{aligned}
$$

Here,

$$
\begin{aligned}
\Delta(\lambda_i)_{j+1/2,k} &:= (\lambda_i^+)_{j+1/2,k} - (\lambda_i^-)_{j+1/2,k},\\
\Delta(\mu_i)_{j,k+1/2} &:= (\mu_i^+)_{j,k+1/2} - (\mu_i^-)_{j,k+1/2},
\end{aligned}
$$

and

$$
\begin{aligned}
(\lambda_i^+)_{j+1/2,k} &= \max\left\{\lambda_i\big(A(U_{j,k}^{\mathrm{E}})\big), \lambda_i\big(A(U_{j+1,k}^{\mathrm{W}})\big), 0\right\},\\
(\lambda_i^-)_{j+1/2,k} &= \min\left\{\lambda_i\big(A(U_{j,k}^{\mathrm{E}})\big), \lambda_i\big(A(U_{j+1,k}^{\mathrm{W}})\big), 0\right\},\\
(\mu_i^+)_{j,k+1/2} &= \max\left\{\mu_i\big(B(U_{j,k}^{\mathrm{N}})\big), \mu_i\big(B(U_{j,k+1}^{\mathrm{S}})\big), 0\right\},\\
(\mu_i^-)_{j,k+1/2} &= \min\left\{\mu_i\big(B(U_{j,k}^{\mathrm{N}})\big), \mu_i\big(B(U_{j,k+1}^{\mathrm{S}})\big), 0\right\},
\end{aligned}
\tag{2.10}
$$

where $\lambda_1(A) \le \cdots \le \lambda_d(A)$ and $\mu_1(B) \le \cdots \le \mu_d(B)$ are the eigenvalues of the Jacobians $A = \partial F/\partial U$ and $B = \partial G/\partial U$, respectively.

In (2.8)-(2.10), $U_{j,k}^{\mathrm{E}}$, $U_{j+1,k}^{\mathrm{W}}$ and $U_{j,k}^{\mathrm{N}}$, $U_{j,k+1}^{\mathrm{S}}$ are the one-sided values of U at the cell interfaces $(x,y) = (x_{j+1/2} \pm 0, y_k)$ and $(x,y) = (x_j, y_{k+1/2} \pm 0)$, respectively. In order to achieve fifth-order accuracy, $U_{j,k}^{\mathrm{E(W)}}$ and $U_{j,k}^{\mathrm{N(S)}}$ are, as in the 1-D case, approximated either using the fifth-order WENO-Z interpolant applied to the local characteristic variables in the x- and y-directions, respectively, or with the help of the adaptive strategy, which we will introduce in Section 4.

3. A New Local Smoothness Indicator (LSI)

In this section, we introduce a very simple LSI, which we will later use as a base for a scheme adaption strategy.

We first consider a function $\psi(\cdot, t)$ and introduce the following quantity:

$$D^{\psi}(\cdot, t - \tau) := \frac{1}{2}\left|\psi(\cdot, t - 2\tau) - 2\psi(\cdot, t - \tau) + \psi(\cdot, t)\right|, \tag{3.1}$$

where $\tau > 0$ and $\cdot$ stand for a certain spatial coordinate. If ψ is smooth, then one can use the Taylor expansion about the point $(\cdot, t - \tau)$ to obtain

$$D^{\psi}(\cdot, t - \tau) = \frac{\tau^2}{2}\psi_{tt}(\cdot, t - \tau) + \mathcal{O}(\tau^4). \tag{3.2}$$

This suggests that for piecewise smooth ψ the magnitude of D^{ψ} is proportional to τ^2 in the areas where ψ is smooth and is $\mathcal{O}(1)$ elsewhere.

In order to design an LSI based on (3.1), we proceed as follows. We begin with the 1-D case, denote by $U(t) := \{U_j(t)\}$, and let $\mathscr{L}[U(t)]$ be the nonlinear operator representing the right-hand side (RHS) of (2.1). Assuming that the computed solution is available at a certain discrete time level $t = t^n$, we evolve it to the next time level $t^{n+1} := t^n + \Delta t^n$ by numerically integrating the ODE system (2.1) using the three-stage third-order SSP Runge-Kutta method, which reads as (see [24, 25])

$$\begin{aligned}
U^{(1)}(t^n) &= U^{(0)}(t^n) + \Delta t^n \mathscr{L}\left[U^{(0)}(t^n)\right], \\
U^{(2)}(t^n) &= \frac{3}{4}U^{(0)}(t^n) + \frac{1}{4}\left(U^{(1)}(t^n) + \Delta t^n \mathscr{L}\left[U^{(1)}(t^n)\right]\right), \\
U^{(3)}(t^n) &= \frac{1}{3}U^{(0)}(t^n) + \frac{2}{3}\left(U^{(2)}(t^n) + \Delta t^n \mathscr{L}\left[U^{(2)}(t^n)\right]\right),
\end{aligned} \tag{3.3}$$

where $U^{(0)}(t^n) := U(t^n)$, $U^{(1)}(t^n)$ and $U^{(2)}(t^n)$ are the intermediate stage solutions, which are lower-order approximations of U at time levels t^{n+1} and $t^{n+1/2} := t^n + \Delta t^n/2$, respectively, and $U^{(3)}(t^n) := U(t^{n+1})$. In (3.3), the time step Δt^n is selected based on the following CFL-based stability restriction:

$$\Delta t^n \leq \frac{\Delta x}{2a}, \quad a := \max_j\left\{\max\left((\lambda_d^+)_{j+1/2}, -(\lambda_1^-)_{j+1/2}\right)\right\}. \tag{3.4}$$

Next, we introduce quantities $\psi_j^{(\ell)}(t^n) := \psi(U_j^{(\ell)}(t^n))$, $\ell = 0, 1, 2, 3$, and the corresponding LSI based on (3.1) with $\tau = \Delta t^n/2$

$$D_j^{\psi}(t^n) = \frac{1}{2}\left|\psi_j^{(0)}(t^n) - 2\psi_j^{(2)}(t^n) + \psi_j^{(3)}(t^n)\right|. \tag{3.5}$$

Similarly, the 2-D LSI is given by

$$D_{j,k}^{\psi}(t^n) = \frac{1}{2}\left|\psi_{j,k}^{(0)}(t^n) - 2\psi_{j,k}^{(2)}(t^n) + \psi_{j,k}^{(3)}(t^n)\right|, \tag{3.6}$$

where $\psi_{j,k}(t^n) := \psi(U_{j,k}^{(\ell)}(t^n))$, $\ell = 0, 1, 2, 3$.

Remark 3.1. We note that in the formulae (3.5) and (3.6) for the LSI we have not used $\psi_j^{(1)}(t^n)$ and $\psi_{j,k}^{(1)}(t^n)$ as these values are lower-order approximations of the quantities, which are more accurately approximated by $\psi_j^{(3)}(t^n)$ and $\psi_{j,k}^{(3)}(t^n)$, respectively.

While the computation in (3.2) is based on the smoothness of ψ, the LSIs (3.5) and (3.6) can, in principle, be used for detecting rough areas of nonsmooth computed solutions. However, before these LSIs can be used for the development of the robust adaptation strategies, one may need to smear the introduced quantities in space by introducing

$$\overline{D}_j^{\psi}(t^n) := \frac{1}{6}\left[D_{j-1}^{\psi}(t^n) + 4D_j^{\psi}(t^n) + D_{j+1}^{\psi}(t^n)\right] \tag{3.7}$$

and

$$\overline{D}_{j,k}^{\psi}(t^n) = \frac{1}{36}\left[D_{j-1,k-1}^{\psi}(t^n) + D_{j-1,k+1}^{\psi}(t^n) + D_{j+1,k-1}^{\psi}(t^n) + D_{j+1,k+1}^{\psi}(t^n)\right.$$
$$\left. + 4\left(D_{j-1,k}^{\psi}(t^n) + D_{j,k-1}^{\psi}(t^n) + D_{j,k+1}^{\psi}(t^n) + D_{j+1,k}^{\psi}(t^n)\right) + 16D_{j,k}^{\psi}(t^n)\right]$$

in the 1-D and 2-D cases, respectively.

In order to verify the plausibility of possible adaptation strategies based on the introduced LSI, we measure its size in the following numerical example in which we compute the solution of a benchmark using the fully limited A-WENO scheme that employs the WENO-Z interpolant throughout the entire computational domain (see Section 2.1).

Example 3.1 (Sod Shock-Tube Problem for Euler Equations of Gas Dynamics)**.** We consider the 1-D Euler equations of gas dynamics, which reads as

$$\begin{aligned}
\rho_t + (\rho u)_x &= 0, \\
(\rho u)_t + (\rho u^2 + p)_x &= 0, \\
E_t + [u(E+p)]_x &= 0,
\end{aligned} \tag{3.8}$$

where ρ, u, p, and E are the density, velocity, pressure, and total energy, respectively. The system (3.8) is completed through the following equations of state:

$$p = (\gamma - 1)\left[E - 1/2\rho u^2\right], \tag{3.9}$$

where the parameter γ represents the specific heat ratio (we take $\gamma = 1.4$). We consider the following initial conditions [59]:

$$(\rho, u, p)(x, 0) = \begin{cases} (1, 0, 1.0), & x < 0.5, \\ (0.125, 0, 0.1), & x > 0.5, \end{cases} \tag{3.10}$$

prescribed in the interval $[0, 1]$ subject to the free boundary conditions.

We compute the numerical solution by the A-WENO scheme introduced in Section 2.1 until the final time $t = 0.16$ on a uniform mesh with $\Delta x = 1/100$. In Fig. 1, we plot the
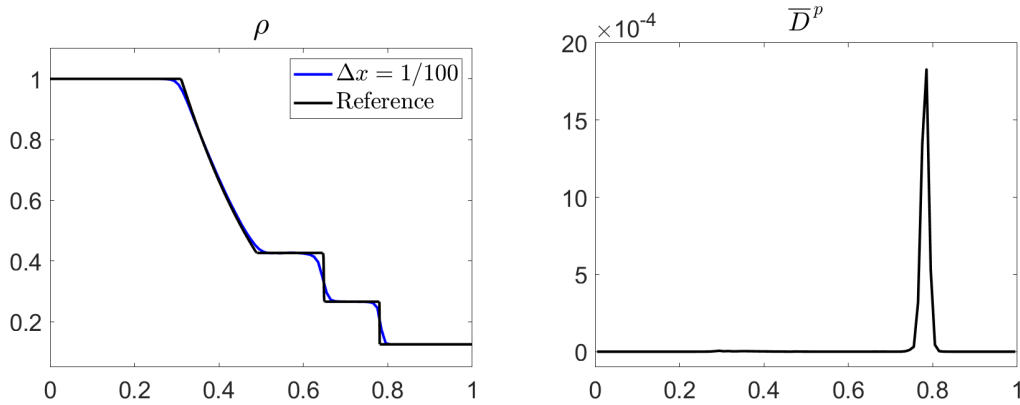
Figure 1: Density (left) and the corresponding values of the pressure-based LSI (right).

obtained density together with the reference solution computed on a much finer uniform mesh with $\Delta x = 1/4000$ and the pressure-based LSI ($\overline{D}_j^p$ defined in (3.7) with $\psi = p$) computed at the final time step. As one can see, the LSI can detect the shock wave's location and indicate the area of a rarefaction corner. At the same time, the LSI values in the contact discontinuity neighborhood are very small. If, however, one is interested in identifying contact discontinuities as well, one can use the density-based LSI ($\overline{D}_j^\rho$ defined in (3.7) with $\psi = \rho$).

In order to investigate the plausibility of the LSI-based adaptive strategies, we compute the numerical solutions on a sequence of uniform meshes with $\Delta x = 1/200, 1/400, 1/800,$ $1/1600, 1/3200, 1/6400,$ and measure the asymptotic behavior of the LSI in different parts of the computational domain. The obtained results are reported in Table 1, where one can observe quite significant differences in the order of magnitude of the LSI. For example, on the mesh with $\Delta x = 1/200$, the local maxima of the $\overline{D}^P$ are $\sim 10^{-6}$ near the rarefaction corner and in a smooth region within the rarefaction wave, $\sim 10^{-7}$ near the contact discontinuity, and $\sim 10^{-3}$ at the shock (the last local maximum is, in fact, the global maximum of $\overline{D}^P$). One can also see that away from the shock, the LSI decays when the mesh is refined. The rate of decay is second-order in the smooth region and about the first-order near the rarefaction corner. In the contact wave area, the LSI is very small, and when the coarse mesh is refined, the LSI decays very rapidly there. At the same time, near the shock, the size of $\overline{D}^P$ is practically independent of the mesh size, as expected. This suggests that the proposed LSI can be used as an efficient and accurate tool to detect shocks and other rough parts of the computed solution except for the isolated contact waves, which can be treated in the same way as smooth parts of the computed solution; see the description of the adaption strategy we propose in the next section.

4. Scheme Adaption

In this section, we develop a scheme adaption strategy based on the LSIs from Section 3 and the A-WENO schemes described in Section 2. This will lead to new adaptive A-WENO

Table 1: Local and global maxima of $\overline{D}^p$ and the corresponding rates of change.

Δx	$\max\limits_{a \leq x_j \leq b} \overline{D}_j^p$	Rate	$\max\limits_{a \leq x_j \leq b} \overline{D}_j^p$	Rate
	Rarefaction corner, $a = 0.25, b = 0.35$		Smooth subregion, $a = 0.35, b = 0.45$	
1/100	7.94e-06	–	3.87e-06	–
1/200	2.86e-06	1.47	1.09e-06	1.83
1/400	1.28e-06	1.17	2.72e-07	2.01
1/800	4.81e-07	1.41	6.75e-08	2.01
1/1600	2.27e-07	1.08	1.66e-08	2.02
1/3200	9.76e-08	1.22	4.14e-09	2.01
1/6400	4.43e-08	1.14	1.03e-09	2.00
	Contact wave, $a = 0.6, b = 0.7$		Everywhere (Shock), $a = 0, b = 1$	
1/100	6.59e-07	–	2.58e-03	–
1/200	1.33e-07	2.31	2.36e-03	0.13
1/400	1.54e-09	6.43	1.82e-03	0.38
1/800	6.55e-10	1.23	2.37e-03	-0.38
1/1600	3.50e-10	0.90	5.76e-04	2.04
1/3200	2.00e-10	0.80	2.00e-03	-1.79
1/6400	8.28e-11	1.27	2.39e-03	-0.26

schemes, in which the WENO-Z interpolation will only be used in the rough areas indicated by the LSI.

One-Dimensional Algorithm. Assume that $U_j(t^n) = U_j^{(3)}(t^{n-1})$, $U_j(t^{n-1}) = U_j^{(0)}(t^{n-1})$, and $U_j^{(2)}(t^{n-1})$ are available for all j. We then compute the LSI values given by (3.7) and identify the rough areas as follows. We first find all of the points $x = x_j$ at which

$$\overline{D}_j^\psi(t^{n-1}) > \mathtt{C}(\Delta t^{n-1})^{\frac{3}{2}}, \tag{4.1}$$

where $\mathtt{C}$ is a positive tunable constant to be selected for each problem at hand, and presume that the solution at time $t = t^{n-1/2}$ is rough there. Due to the finite speed of propagation and the CFL condition (3.4), one may presume that the solution at the time interval $[t^n, t^{n+1}]$ (that is, at all of the three Runge-Kutta stages (3.3)) is rough at the nearby points $x_{j\pm1/2}$ and $x_{j\pm3/2}$.

After identifying each of the points $x_{j+1/2}$ as either rough or smooth, we compute either nonlimited $\breve{U}_{j+1/2}^\pm$ or limited $\widetilde{U}_{j+1/2}^\pm$ point values there, and then evaluate the finite-volume numerical fluxes needed in (2.1)-(2.2) (and hence in (3.3)) by

$$\mathscr{F}_{j+1/2}^{\mathrm{FV}} = \begin{cases} \mathscr{F}_{j+1/2}^{\mathrm{FV}}\big(\breve{U}_{j+1/2}^-, \breve{U}_{j+1/2}^+\big), & \text{if } x_{j+1/2} \text{ is rough,} \\ \mathscr{F}_{j+1/2}^{\mathrm{FV}}\big(\widetilde{U}_{j+1/2}^-, \widetilde{U}_{j+1/2}^+\big), & \text{if } x_{j+1/2} \text{ is smooth.} \end{cases}$$

Two-Dimensional Algorithm.   An extension of the 1-D scheme adaption algorithm to the 2-D case is relatively straightforward.

The main component of the 2-D algorithm is identifying the rough parts of the solution, in which the one-sided interpolated values are to be computed using the WENO-Z interpolant. As in the 1-D case, this is done using the LSI. Namely, we presume that the solution at time $t = t^{n-1/2}$ is rough in all of the cells $C_{j,k}$, in which

$$\overline{D}_{j,k}^{\psi}(t^{n-1}) > \mathtt{C}(\Delta t^{n-1})^{\frac{3}{2}}. \tag{4.2}$$

Then, due to the finite speed of propagation and the appropriate CFL condition with the CFL number $1/2$, one may presume that the solution at the time interval $[t^n, t^{n+1}]$ is rough at the nearby points $(x_{j\pm1/2}, y_{k\pm1})$, $(x_{j\pm1/2}, y_k)$, $(x_{j\pm3/2}, y_k)$ and $(x_{j\pm1}, y_{k\pm1/2})$, $(x_j, y_{k\pm1/2})$, $(x_j, y_{k\pm3/2})$.

Equipped with the information about the rough and smooth parts of the computed solutions, we proceed with the proposed adaption strategy and compute either nonlimited $\breve{U}_{j,k}^{\mathrm{E(W,N,S)}}$ or limited $\widetilde{U}_{j,k}^{\mathrm{E(W,N,S)}}$ point values there, and then evaluate the finite-volume numerical fluxes needed in (2.6)-(2.7) by

$$\mathscr{F}_{j+1/2,k}^{\mathrm{FV}} = \begin{cases} \mathscr{F}_{j+1/2,k}^{\mathrm{FV}}\big(\breve{U}_{j,k}^{\mathrm{E}}, \breve{U}_{j+1,k}^{\mathrm{W}}\big), & \text{if} \quad (x_{j+1/2}, y_k) \quad \text{is rough,} \\ \mathscr{F}_{j+1/2,k}^{\mathrm{FV}}\big(\widetilde{U}_{j,k}^{\mathrm{E}}, \widetilde{U}_{j+1,k}^{\mathrm{W}}\big), & \text{if} \quad (x_{j+1/2}, y_k) \quad \text{is smooth,} \end{cases}$$

$$\mathscr{G}_{j,k+1/2}^{\mathrm{FV}} = \begin{cases} \mathscr{G}_{j,k+1/2}^{\mathrm{FV}}\big(\breve{U}_{j,k}^{\mathrm{N}}, \breve{U}_{j,k+1}^{\mathrm{S}}\big), & \text{if} \quad (x_j, y_{k+1/2}) \quad \text{is rough,} \\ \mathscr{G}_{j,k+1/2}^{\mathrm{FV}}\big(\widetilde{U}_{j,k}^{\mathrm{N}}, \widetilde{U}_{j,k+1}^{\mathrm{S}}\big), & \text{if} \quad (x_j, y_{k+1/2}) \quad \text{is smooth.} \end{cases}$$

Remark 4.1. The fact that the constants $\mathtt{C}$ in (4.1) and (4.2) must be tuned is a weak point of our adaption strategy. One may, however, tune $\mathtt{C}$ on a coarse mesh and then use the same value of $\mathtt{C}$ on finer meshes to minimize an extra computational cost as it was done, e.g., in [36] in the context of an adaptive artificial viscosity method. The plausibility of this strategy in the current scheme adaption algorithm is supported by a numerical experiment; see Example 5.1 in Section 5.1 below.

Remark 4.2. As no past time solution is available at the first time step, at $t^0 = 0$, we complete the first evolution step using a fully limited A-WENO scheme that employs the WENO-Z interpolation throughout the entire computational domain.

5. Numerical Examples

In this section, we test the developed adaption strategy on several numerical examples. To this end, we apply the adaptive A-WENO schemes to several initial-boundary value problems for the 1-D and 2-D Euler equations of gas dynamics and compare their performance with the fully limited A-WENO schemes. In the rest of this section, we will refer to the proposed adaptive A-WENO schemes as to adaptive schemes and the fully limited A-WENO schemes as to limited schemes.

In all of the examples below, the specific heat ratio is $\gamma = 1.4$ (except for Example 5.11, where $\gamma = 5/3$), and the CFL number is 0.45.

5.1. One-dimensional examples

Example 5.1 (1-D Accuracy Test). In the first example taken from [13, 37], we consider the (3.8)-(3.10) subject to the following smooth initial data:

$$u(x,0) = \sin\left(\frac{\pi x}{5} + \frac{\pi}{4}\right), \quad \rho(x,0) = \left[\frac{\gamma-1}{2\sqrt{\gamma}}(u(x,0)+10)\right]^{\frac{2}{\gamma-1}}, \quad p(x,0) = \rho^{\gamma}(x,0).$$

We impose periodic boundary conditions and compute the numerical solution on the computational domain $[0,10]$ on a sequence of uniform meshes with $\Delta x = 1/10$, $1/20$, $1/40$, $1/80$, $1/160$, $1/320$, $1/640$ until the final time $t = 0.1$ using the adaptive scheme with $\texttt{C} = 0.1$. Since we use a fifth-order spatial discretization and only third-order time integrator, we select $\Delta t \sim (\Delta x)^{5/3}$ in order to be able to achieve the overall fifth order of accuracy.

We then compute L^1-errors and estimate the experimental convergence rates using the following Runge formulae, which are based on the solutions computed on the three consecutive uniform grids with the mesh sizes Δx, $2\Delta x$, and $4\Delta x$ and denoted by $(\cdot)^{\Delta x}$, $(\cdot)^{2\Delta x}$, and $(\cdot)^{4\Delta x}$, respectively:

$$\text{Error}(\Delta x) \approx \frac{\delta_{12}^2}{|\delta_{12} - \delta_{24}|}, \quad \text{Rate}(\Delta x) \approx \log_2\left(\frac{\delta_{24}}{\delta_{12}}\right).$$

Here, $\delta_{12} := \|(\cdot)^{\Delta x} - (\cdot)^{2\Delta x}\|_{L^1}$ and $\delta_{24} := \|(\cdot)^{2\Delta x} - (\cdot)^{4\Delta x}\|_{L^1}$. The computed L^1-errors and corresponding convergence rates for the density, momentum, and total energy are reported in Table 2, where one can clearly see that the fifth order of accuracy is achieved.

Table 2: Example 5.1: The L^1-errors and experimental convergence rates for the density (ρ), momentum (ρu), and total energy (E).

Δx	ρ		ρu		E	
	Error	Rate	Error	Rate	Error	Rate
1/40	3.87e-05	4.75	1.27e-04	4.76	5.61e-04	4.76
1/80	1.03e-06	5.23	3.37e-06	5.23	1.49e-05	5.23
1/160	3.83e-08	4.75	1.25e-07	4.75	5.54e-07	4.75
1/320	1.20e-09	4.99	3.93e-09	4.99	1.74e-08	4.99
1/640	3.82e-11	4.98	1.25e-10	4.98	5.53e-10	4.98

Example 5.2 (Sod Shock-Tube Problem). In the second example, we once again consider (3.8)-(3.10) subject to the free boundary conditions and compute the numerical solution until the final time $t = 0.16$ using both the limited and adaptive schemes. In this example, we take $\texttt{C} = 0.05$ while implementing the scheme adaption strategy. The obtained solutions, computed on a uniform mesh with $\Delta x = 1/200$ and the corresponding reference solution computed by the limited scheme on a much finer mesh with $\Delta x = 1/4000$ are presented in Fig. 2. We also plot the LSI $\overline{D}^p$ and $0.05(\Delta t)^{3/2}$ along with $\log_{10} \overline{D}^p$ and

$\log_{10}(0.05(\Delta t)^{3/2})$, computed during the adaptive scheme evolution at the final time moment in Fig. 3. One can observe that the computed LSI can capture the shock wave position accurately, and the results obtained by the adaptive scheme are sharper than those obtained by the limited scheme, even though there are small oscillations near the contact wave captured by the adaptive scheme. It is also instructive to point out that choosing the adaption constant C on a coarse mesh is a robust strategy. This is evident from the graphs of $\log_{10} \overline{D}^p$ and $\log_{10}(0.05(\Delta t)^{3/2})$ depicted in Figs. 3 (right) and 4. The presented results illustrate that the rough parts of the computed solutions can be accurately identified using (4.1), while the same constant $C = 0.05$ is used on three different meshes.

Example 5.3 (Shock-Bubble Iteration Problem). In the third example taken from [39], we consider the shock-bubble interaction problem. The initial data for the 1-D Euler equations (3.8)-(3.9),

$$(\rho, u, p)(x, 0) = \begin{cases} (13.1538, 0, 1), & |x| < 0.25, \\ (1.3333, -0.3535, 1.5), & x > 0.75, \\ (1, 0, 1), & \text{otherwise} \end{cases}$$

correspond to a left-moving shock, initially located at $x = 0.75$, and a bubble with a radius of 0.25, initially located at the origin.

We compute the numerical solution in the computational domain $[-1, 1]$ on the uniform mesh with $\Delta x = 1/100$ and impose the solid wall boundary conditions at $x = -1$ and free boundary conditions at $x = 1$. In Figs. 5 and 6, we plot the numerical solutions at the final time $t = 3$ obtained by the limited and adaptive (with $C = 0.0015$) schemes. These solutions are compared with the corresponding reference solutions computed by the limited scheme on a much finer mesh with $\Delta x = 1/2000$. In Fig. 7, the graphs of LSI $\overline{D}^p$ and $0.0015(\Delta t)^{3/2}$ are depicted along with their logarithm forms. As one can observe, the LSI accurately captures the position of the shock waves, and the results obtained by the adaptive scheme are a little sharper compared to those obtained by the limited counterpart.

Example 5.4 (Shock-Entropy Wave Interaction Problem). In the fourth example taken from [57], we consider the shock-entropy wave interaction problem. The system (3.8)-(3.9) is numerically solved subject to the following initial condition:

$$(\rho, u, p)(x, 0) = \begin{cases} (1.51695, 0.523346, 1.805), & x < -4.5, \\ (1 + 0.1 \sin(20x), 0, 1), & x > -4.5, \end{cases}$$

which corresponds to a forward-facing shock wave of Mach number 1.1 interacting with high-frequency density perturbations, that is, as the shock wave moves, the perturbations spread ahead.

We compute the numerical solution using both the limited and adaptive schemes with $C = 0.006$ in the computational domain $[-5, 5]$ covered by a uniform mesh with $\Delta x = 1/40$ and implement free boundary conditions. The numerical results at time $t = 5$ are presented in Fig. 8 along with the corresponding reference solution computed by the limited scheme on a much finer mesh with $\Delta x = 1/800$. As in the previous example, we also plot (in Fig. 9)
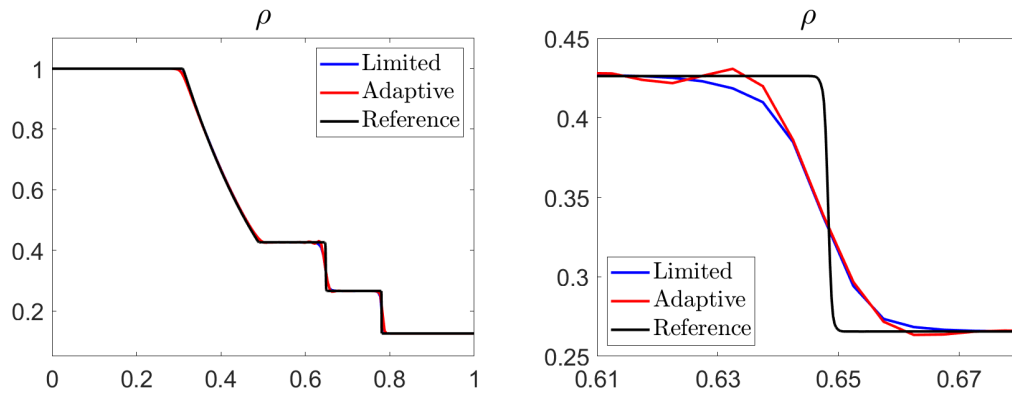
Figure 2: Example 5.2: Density ρ computed by the limited and adaptive schemes (left) and zoom at $x \in [0.61, 0.68]$ (right).
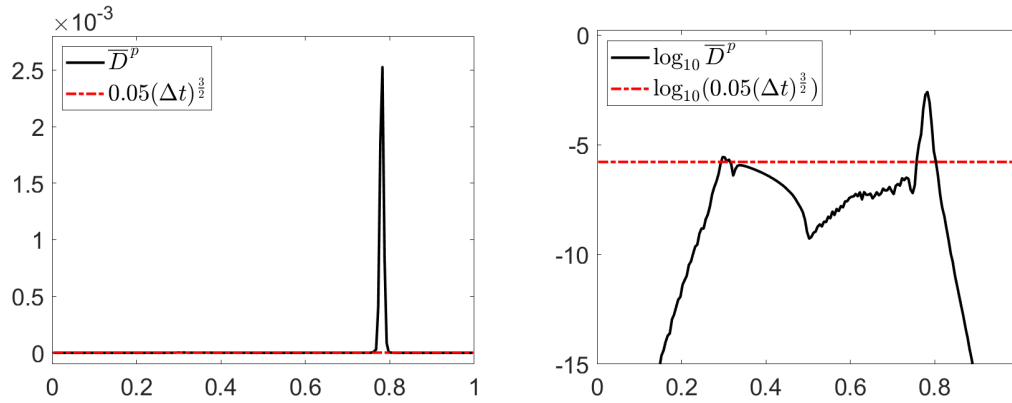

Figure 3: Example 5.2: $\overline{D}^p$ and $0.05(\Delta t)^{3/2}$ (left) and $\log_{10} \overline{D}^p$ and $\log_{10}(0.05(\Delta t)^{3/2})$ (right) for $\Delta x = 1/200$.
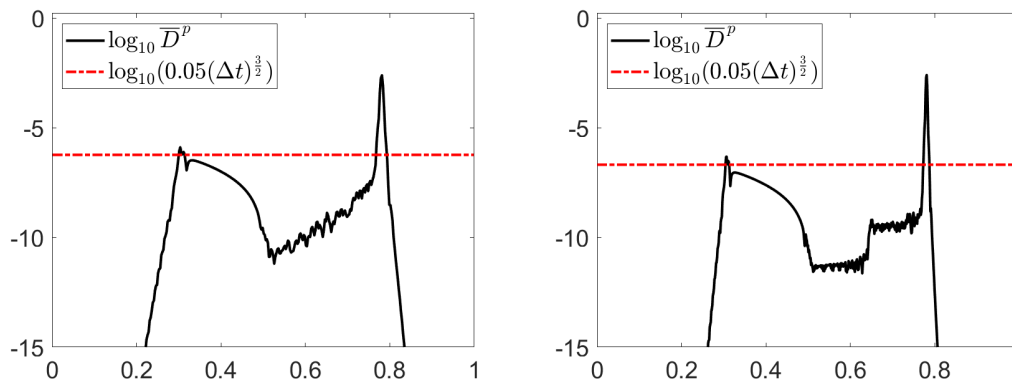

Figure 4: Example 5.2: $\log_{10} \overline{D}^p$ and $\log_{10}(0.05(\Delta t)^{3/2})$ for $\Delta x = 1/400$ (left) and $1/800$ (right).
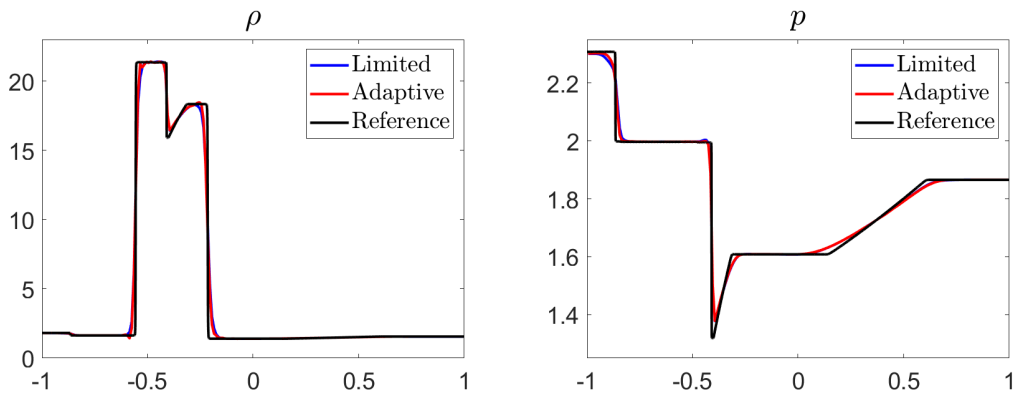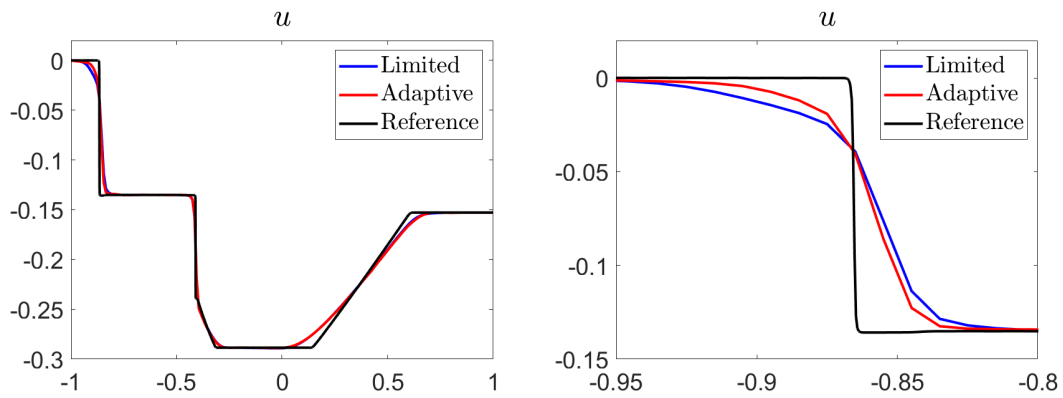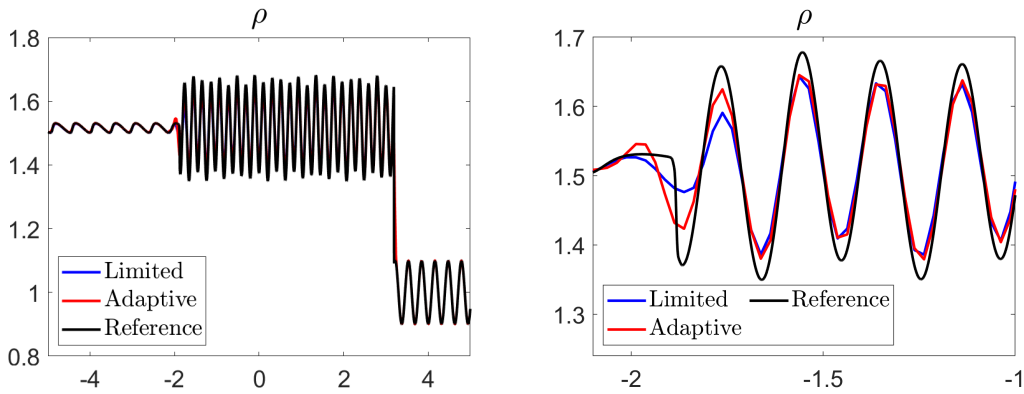
Figure 5: Example 5.3: Density ρ (left) and pressure p (right) computed by the limited and adaptive schemes.

Figure 6: Example 5.3: Velocity u computed by the limited and adaptive schemes (left) and zoom at $x \in [-0.95, -0.8]$ (right).
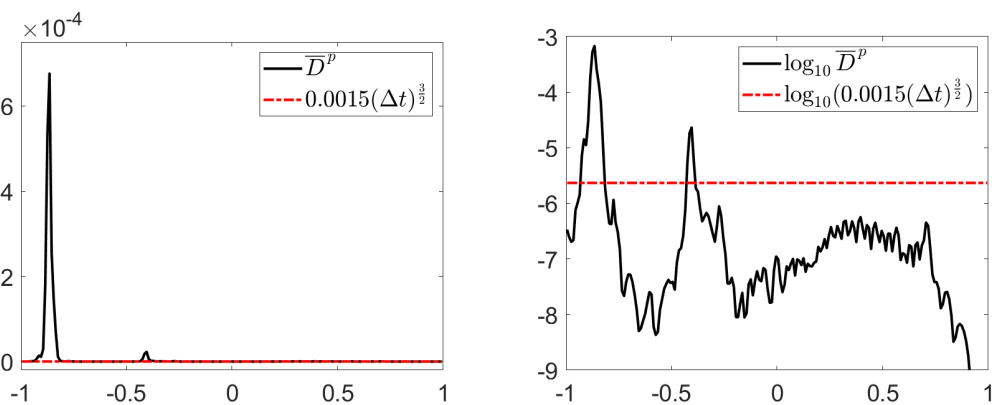
Figure 7: Example 5.3: $\overline{D}^p$ and $0.0015(\Delta t)^{3/2}$ (left) and the corresponding logarithmic quantities (right).

Figure 8: Example 5.4: Density ρ computed by the limited and adaptive schemes (left) and zoom at $x \in [-2.1, -1]$ (right).
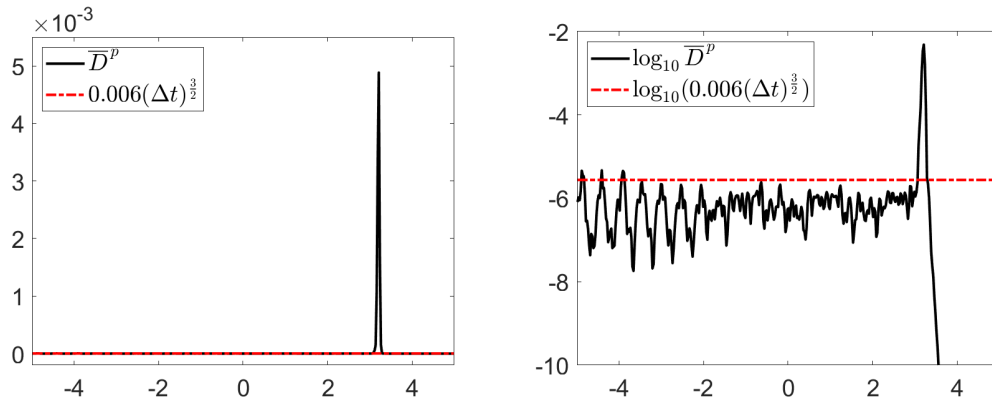
Figure 9: Example 5.4: $\overline{D}^p$ and $0.006(\Delta t)^{3/2}$ (left) and the corresponding logarithmic quantities (right).

the graphs of the LSI $\overline{D}^p$ and $0.006(\Delta t)^{3/2}$ together with $\log_{10} \overline{D}^p$ and $\log_{10}(0.006(\Delta t)^{3/2})$. One can observe that the LSI can capture the position of the shock waves accurately, and the results obtained by the adaptive scheme are non-oscillatory and slightly sharper than those obtained by the limited scheme.

Example 5.5 (Shock-Density Wave Interaction Problem). In the last 1-D example taken from [58], we consider the shock-density wave interaction problem. The initial data,

$$(\rho, u, p)(x, 0) = \begin{cases} \left(\dfrac{27}{7}, \dfrac{4\sqrt{35}}{9}, \dfrac{31}{3} \right), & x < -4, \\ (1 + 0.2\sin(5x), 0, 1), & x > -4 \end{cases}$$

are prescribed in the computational domain $[-5, 15]$ subject to the free boundary conditions.

We compute the numerical solution by the limited and adaptive (with $\mathtt{C} = 0.04$) schemes on the uniform mesh with $\Delta x = 1/20$ until the final time $t = 5$ and present the obtained
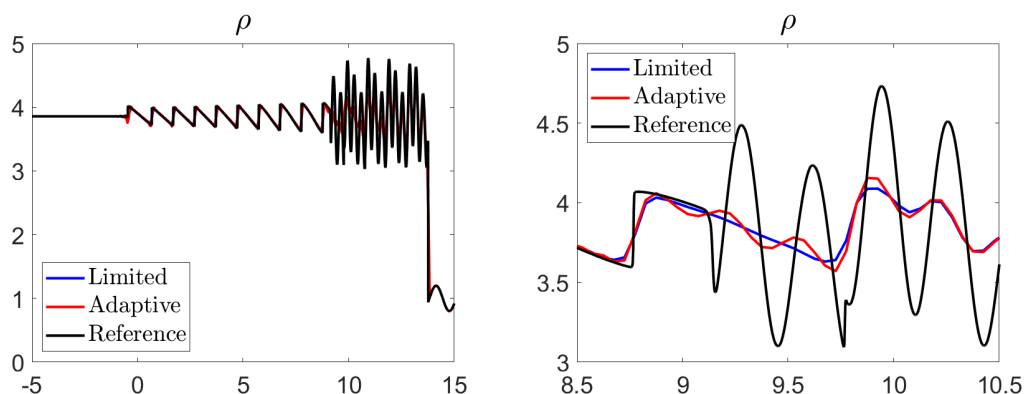
Figure 10: Example 5.5: Density ρ computed by the limited and adaptive schemes (left) and zoom at $x \in [8, 10]$ (right).
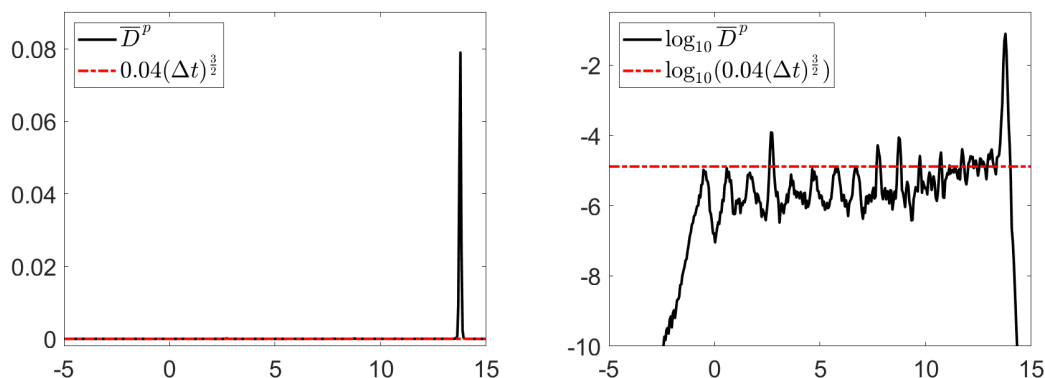

Figure 11: Example 5.5: $\overline{D}^p$ and $0.04(\Delta t)^{3/2}$ (left) and the corresponding logarithmic quantities (right).

numerical results in Fig. 10 together with the corresponding reference computed by the limited scheme on a much finer mesh with $\Delta x = 1/400$. We also plot $\overline{D}^p$ and $0.04(\Delta t)^{3/2}$ together with $\log_{10} \overline{D}^p$ and $\log_{10}(0.04(\Delta t)^{3/2})$ in Fig. 11. It can be seen clearly that the LSI can accurately capture the position of the shock waves, and the adaptive scheme produces slightly sharper results compared to those obtained by the limited scheme.

Remark 5.1. It is instructive to compare the computational costs of the studied limited and adaptive A-WENO schemes. To this end, we have measured the CPU times consumed by both schemes. The results obtained for the four studied 1-D examples are reported in Table 3, where we show the relative CPU time consumption of the adaptive A-WENO scheme relative to the fully limited one. As one can see, the proposed adaptive the scheme is more efficient than the fully limited one. Notice that the numbers in Table 3 are different as the part of the computational domain indicated as rough varies. The CPU times for the adaptive scheme also depend on the values of C: the use of larger C leads to a more efficient but potentially more oscillatory adaptive A-WENO scheme.

Table 3: Examples 5.2-5.5: CPU times consumed by the adaptive A-WENO scheme relative to the fully limited A-WENO scheme.

Example 5.2	Example 5.3	Example 5.4	Example 5.5
66%	76%	66%	67%

5.2. Two-dimensional examples

In this section, we demonstrate the performance of the proposed adaptive A-WENO scheme on several examples for the 2-D Euler equations of gas dynamics, which read as

$$
\begin{aligned}
\rho_t + (\rho u)_x + (\rho v)_y &= 0, \\
(\rho u)_t + (\rho u^2 + p)_x + (\rho u v)_y &= 0, \\
(\rho v)_t + (\rho u v)_x + (\rho v^2 + p)_y &= 0, \\
E_t + [u(E + p)]_x + [v(E + p)]_y &= 0,
\end{aligned}
\tag{5.1}
$$

where v is the y-component of the velocity, and the rest of the notations are the same as in the 1-D case. The system is completed through the following equations of state:

$$
p = (\gamma - 1)\Big[E - \frac{\rho}{2}(u^2 + v^2)\Big].
\tag{5.2}
$$

Example 5.6 (2-D Accuracy Test). In the first 2-D example taken from [13,37], we consider the 2-D Euler equations of gas dynamics subject to the following periodic initial conditions:

$$
\rho(x, y, 0) = 1 + \frac{1}{2}\sin\big(\pi(x + y)\big), \quad u(x, y, 0) \equiv 1, \quad v(x, y, 0) \equiv -0.7, \quad p(x, y, 0) \equiv 1.
$$

The exact solution of this initial value problem is given by

$$
\rho(x, y, t) = 1 + \frac{1}{2}\sin\big[\pi(x + y - 0.3t)\big], \quad u(x, y, t) \equiv 1, \quad v(x, y, t) \equiv -0.7, \quad p(x, y, 0) \equiv 1.
$$

We first compute the numerical solution on the computational domain $[-1, 1] \times [-1, 1]$ until the final time $t = 0.1$ using the adaptive scheme with $C = 0.1$ on a sequence of uniform meshes with $\Delta x = \Delta y = 1/50, 1/100, 1/200, 1/400$, and the time step chosen to be proportional to $(\Delta x)^{5/3}$. We then measure the L^1-errors and compute the corresponding experimental convergence rates for the density. The obtained results are presented in Table 4, where one can see that the fifth order of accuracy is achieved by the proposed adaptive scheme.

Table 4: Example 5.6: The L^1-errors and experimental convergence rates for the density ρ.

$\Delta x = \Delta y$	Error	Rate
1/50	2.49e-07	—
1/100	7.80e-09	4.99
1/200	2.44e-10	5.00
1/400	7.62e-12	5.00

Example 5.7 (2-D Riemann Problem). In the second 2-D example, we consider Configuration 3 of the 2-D Riemann problems from [38] (see also [52, 53, 65]) with the following initial conditions:

$$(\rho, u, v, p)(x, y, 0) = \begin{cases} (1.5, 0, 0, 1.5), & x > 1, \quad y > 1, \\ (0.5323, 1.206, 0, 0.3), & x < 1, \quad y > 1, \\ (0.138, 1.206, 1.206, 0.029), & x < 1, \quad y < 1, \\ (0.5323, 0, 1.206, 0.3), & x > 1, \quad y < 1. \end{cases}$$

We compute the numerical solution until the final time $t = 1$ by the limited and adaptive (with $C = 3$) schemes on the uniform mesh with $\Delta x = \Delta y = 3/2500$ in the computational domain $[0, 1.2] \times [0, 1.2]$ subject to the free boundary conditions. The obtained results are presented in Fig. 12, where one can see that the adaptive scheme outperforms the limited one as it better captures the sideband instability of the jet in the zones of strong along-jet velocity shear and the instability along the jet's neck.
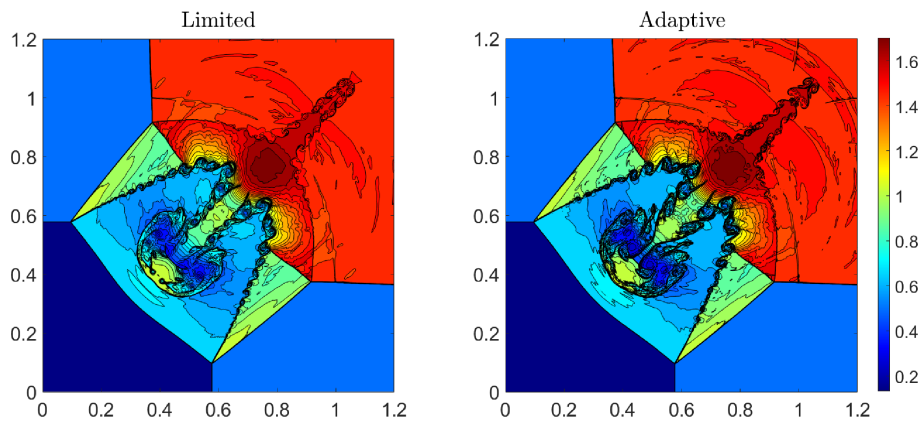

Figure 12: Example 5.7: Density ρ computed by the limited (left) and adaptive (right) schemes.
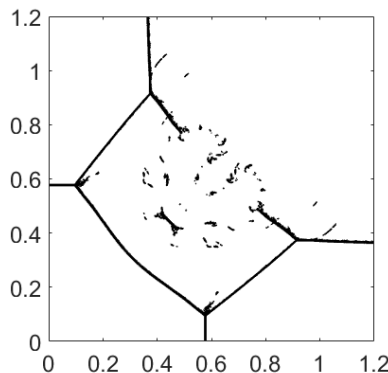

Figure 13: Example 5.7: The limited WENO-Z interpolation is used only in the part of the computational domain indicated by the black color.

In Fig. 13, we show the regions which the LSI detected as rough at the final time. As one can see, the limited WENO-Z interpolation is used only in a small part of the computational domain, mostly around the shocks.

Example 5.8 (Explosion Problem)**.** In this example, we consider the explosion problem taken from [42, 60]. This is a circularly symmetric problem with the following initial conditions:

$$(\rho, u, v, p)(x, y, 0) = \begin{cases} (1, 0, 0, 1), & x^2 + y^2 < 0.16, \\ (0.125, 0, 0, 0.1), & \text{otherwise.} \end{cases} \tag{5.3}$$

We numerically solve the initial value problem (5.1)-(5.3) in the first quadrant, more precisely in the computational domain $[0, 1.5] \times [0, 1.5]$ with the solid wall boundary conditions imposed at $x = 0$ and $y = 0$ and the free boundary conditions set at $x = 1.5$ and $y = 1.5$.

In Fig. 14, the numerical solutions computed by the limited and adaptive (with $C = 1$) schemes on the uniform mesh with $\Delta x = \Delta y = 3/800$ are plotted at the final time $t = 3.2$.
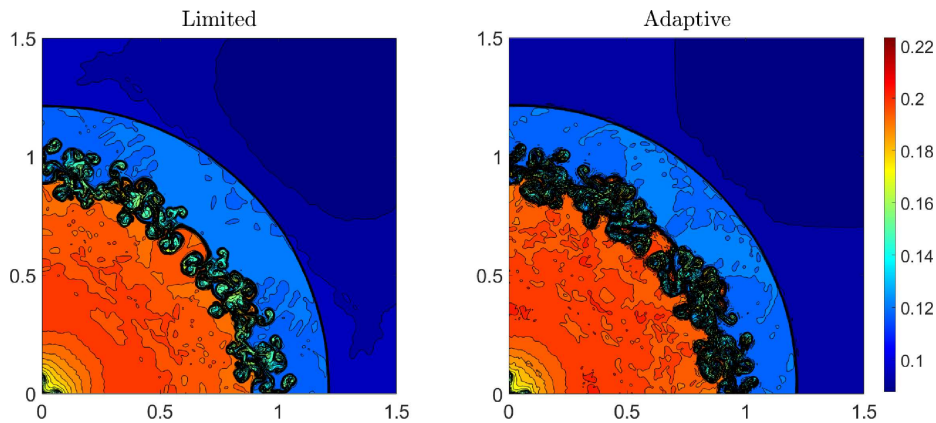

Figure 14: Example 5.8: Density ρ computed by the limited (left) and adaptive (right) schemes.
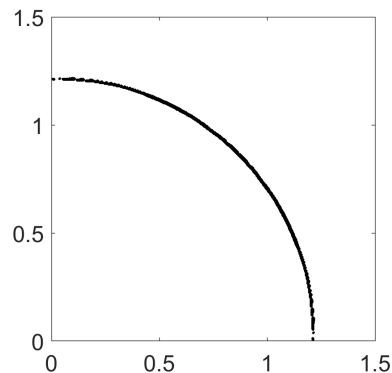

Figure 15: Example 5.8: The limited WENO-Z interpolation is used only in the part of the computational domain indicated by the black color.

The presented results clearly illustrate the advantage of the adaptive approach over the fully limited one, as the contact curve captured by the adaptive scheme is much curlier and the mixing layer is much wider.

In Fig. 15, we show the regions detected at the final time by the LSI as rough and demonstrate that in this example, the limiting is only used along the circular shock.

Example 5.9 (Implosion Problem)**.** In this example taken from [42], we consider the implosion problem with the following initial conditions:

$$(\rho, u, v, p)(x, y, 0) = \begin{cases} (0.125, 0, 0, 0.14), & |x| + |y| < 0.15, \\ (1, 0, 0, 1), & \text{otherwise,} \end{cases} \tag{5.4}$$

prescribed in $[-0.3, 0.3] \times [-0.3, 0.3]$ subject to the solid wall boundary conditions. Due to the symmetry, we numerically solve the initial-boundary value problem (5.1), (5.2), and (5.4) in the first quadrant only, more precisely in the computational domain $[0, 0.3] \times [0, 0.3]$ and impose the solid wall boundary conditions at $x = 0$ and $y = 0$.

In Fig. 16, the numerical solutions computed by the limited and adaptive (with $\mathtt{C} = 3$) schemes on the uniform mesh with $\Delta x = \Delta y = 3/4000$ are plotted at the final time $t = 2.5$. As one can observe, the jet generated by the adaptive scheme propagates further in the direction of $y = x$ than the jet produced by the limited scheme, clearly indicating that the adaptive scheme is substantially less dissipative than the limited scheme.

The domain where the limiters have been used at the final time is presented in Fig. 17, where one can see how the proposed LSI identifies rough areas.

Remark 5.2. It is easy to show that the solution of the studied initial-boundary value problem is symmetric with respect to the axis $y = x$. It is well-known, however, that this symmetry may be destroyed by the roundoff errors when the solution is computed by a low-dissipative high-order scheme. In order to prevent the loss of symmetry, we have used a very simple strategy introduced in [62]: upon completion of each time evolution step, we
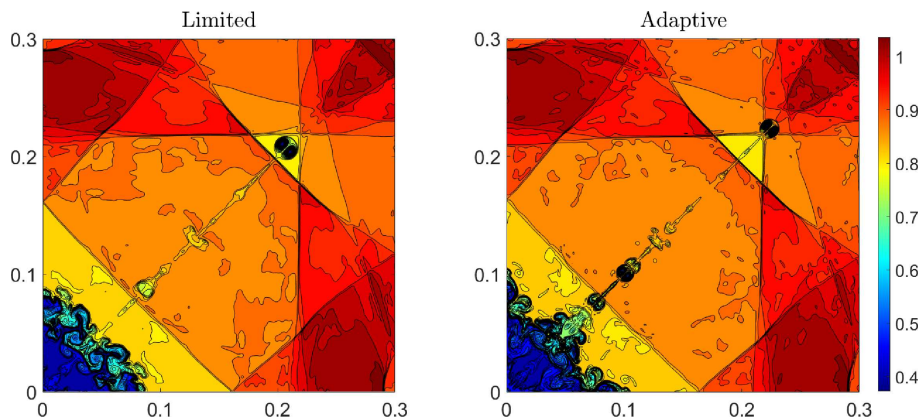

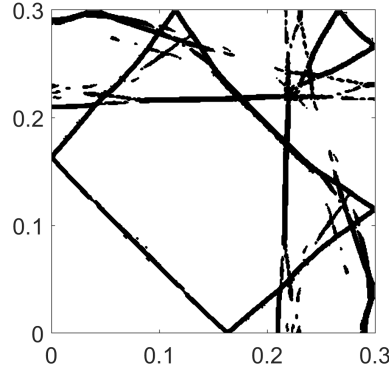Figure 16: Example 5.9: Density ρ computed by the limited (left) and adaptive (right) schemes.

Figure 17: Example 5.9: The limited WENO-Z interpolation is used only in the part of the computational domain indicated by the black color.

replace the computed point values $U_{j,k}$ with $\widehat{U}_{j,k}$, where

$$\widehat{\rho}_{j,k} := \frac{\rho_{j,k} + \rho_{k,j}}{2}, \quad (\widehat{\rho u})_{j,k} := \frac{(\rho u)_{j,k} + (\rho v)_{k,j}}{2},$$
$$\widehat{E}_{j,k} := \frac{E_{j,k} + E_{k,j}}{2}, \quad (\widehat{\rho v})_{j,k} := \frac{(\rho v)_{j,k} + (\rho u)_{k,j}}{2}$$

for all j, k. For more sophisticated symmetry enforcement techniques, we refer the reader to, e.g., [16, 17, 20, 61].

Example 5.10 (KH Instability). In this example taken from [19, 45], we study the KH instability with the following initial conditions:

$$\big(\rho(x,y,0), u(x,y,0)\big) = \begin{cases} (1, -0.5 + 0.5e^{(y+0.25)/L}), & y \in [-0.5, -0.25), \\ (2, 0.5 - 0.5e^{(-y-0.25)/L}), & y \in [-0.25, 0), \\ (2, 0.5 - 0.5e^{(y-0.25)/L}), & y \in [0, 0.25), \\ (1, -0.5 + 0.5e^{(-y+0.25)/L}), & y \in [0.25, 0.5), \end{cases}$$
$$v(x,y,0) = 0.01 \sin(4\pi x), \quad p(x,y,0) \equiv 1.5,$$

where L is a smoothing parameter (here, we take $L = 0.00625$) corresponding to a thin shear interface with a perturbed vertical velocity field v in the conducted simulations. We impose the 1-periodic boundary conditions in both the x- and y-directions, and take the computational domain to be $[-0.5, 0.5] \times [-0.5, 0.5]$.

We compute the numerical solution until the final time $t = 4$ by the limited and adaptive (with $C = 1$) schemes on the uniform mesh with $\Delta x = \Delta y = 1/400$. The numerical results at $t = 1, 2.5, 4$ are presented in Fig. 18. As one can see, at the early time $t = 1$, the vortex sheets in the limited and adaptive results are quite different, and it is hard to draw a definite conclusion based on these results. However, at later times $t = 2.5, 4$, the adaptive
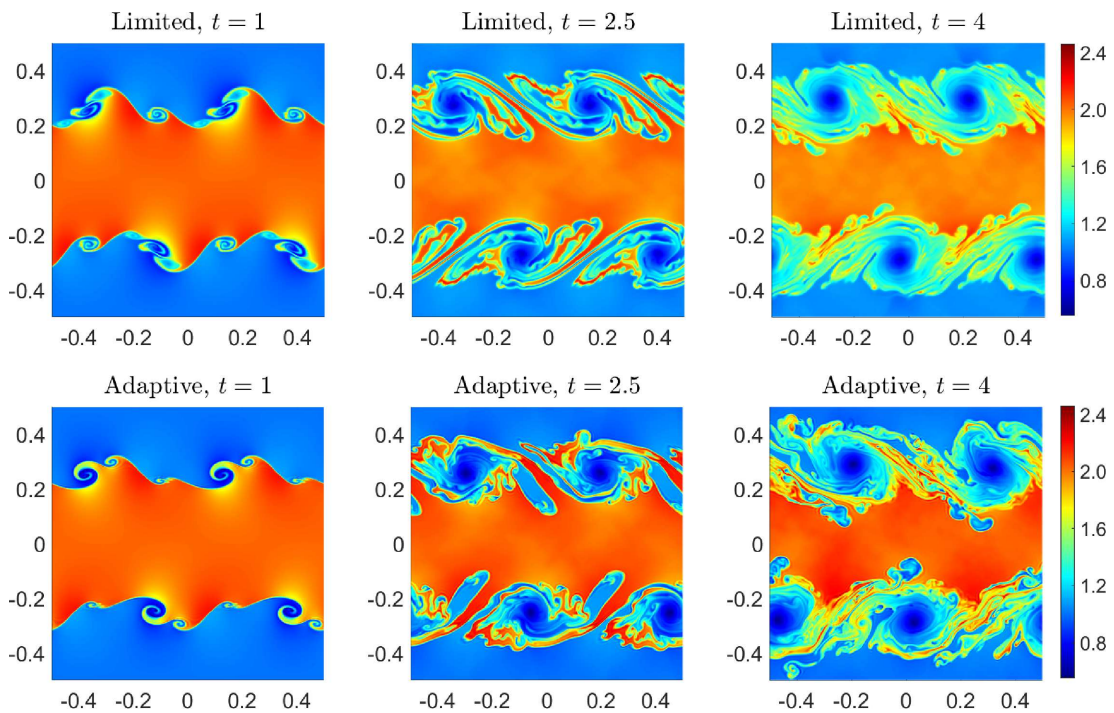
Figure 18: Example 5.10: Time snapshots of the density ρ computed by the limited (top row) and adaptive (bottom row) schemes at $t = 1$ (left column), 2.5 (middle column), and 4 (right column).

scheme produces more complicated vortices and turbulent mixing, which indicates that the adaptive scheme contains less numerical dissipation than the limited scheme.

In addition, in Fig. 19, we plot the solution regions to show that the limiters have been used in a very small part of the computational domain, especially at $t = 4$.

It should also be noted that, as is known, the numerical solutions of the KH instability problem do not converge in the strong sense when the mesh is refined. In fact, the limiting
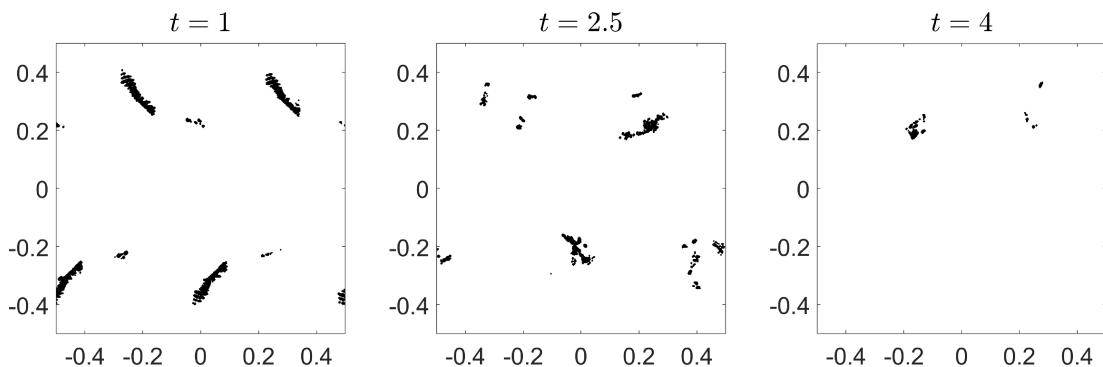

Figure 19: Example 5.10: The limited WENO-Z interpolation is used only in the part of the computational domain indicated by the black color.
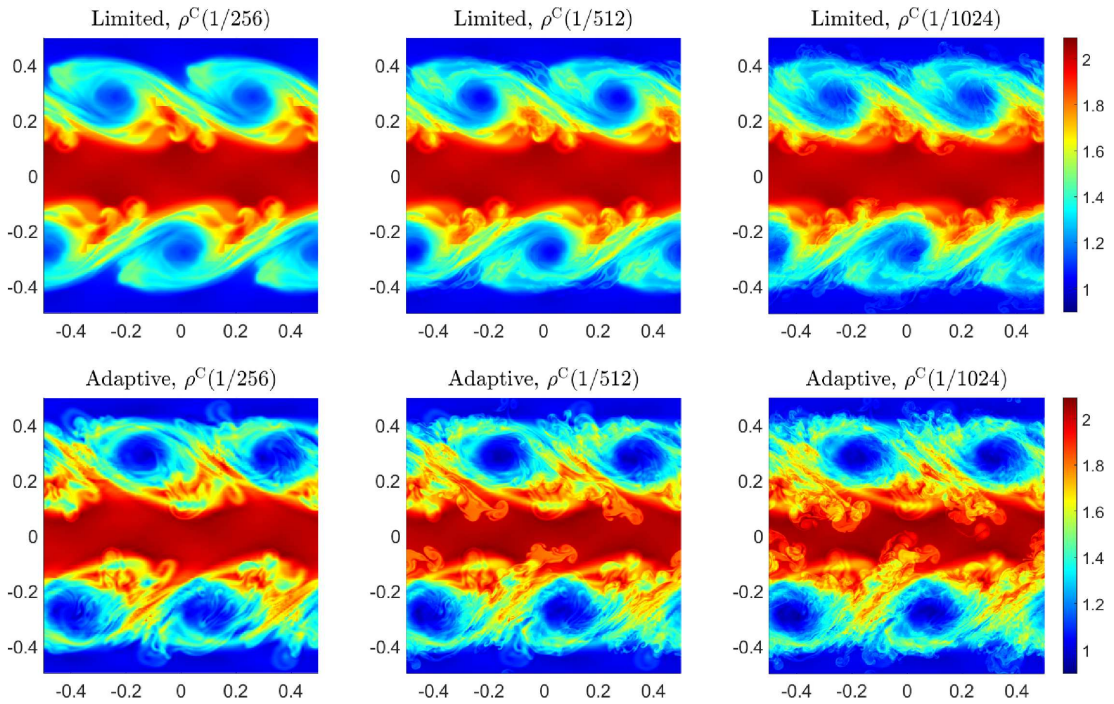
Figure 20: Example 5.10: Cesàro averages of the density $\rho^C(1/2^m)$ computed by the limited (top row) and adaptive (bottom row) schemes for $m = 8$ (left column), 9 (middle column), and 10 (right column).

solution is not a weak solution but a dissipative weak solution; see [18] for more details. Thus, to approximate the limiting solution, we compute the Cesàro averages of the densities obtained at the final time $t = 4$ by the limited and adaptive schemes. To this end, we first introduce a sequence of meshes with the cells of size $1/2^n$, $n = 5, \ldots, 10$, and denote by $\rho(1/2^n)$ the density computed on the corresponding mesh. We then project the obtained coarser mesh solutions with $n = 5, \ldots, m-1$ onto the finer mesh with $n = m$ (the projection is carried out using the dimension-by-dimension WENO-Z interpolation of the density field) and denote the obtained densities still by $\rho(1/2^n)$, $n = 5, \ldots, m$. After this, the Cesàro averages are computed by

$$\rho^C(1/2^m) = \frac{\rho(1/2^5) + \cdots + \rho(1/2^m)}{m-4}, \quad m = 8, 9, 10. \tag{5.5}$$

In Fig. 20, we plot the computed averages at time $t = 4$. One can observe the superiority of the results obtained by the adaptive scheme when it comes to resolving complicated structures.

Example 5.11 (RT Instability). In the last example, we investigate the RT instability. It is a physical phenomenon occurring when a layer of heavier fluid is placed on top of a layer of lighter fluid. To this end, we first modify the 2-D Euler equations of gas dynamics (5.1)-(5.2) by adding the gravitational source terms acting in the positive direction of the y-axis

into the RHS of the system

$$\rho_t + (\rho u)_x + (\rho v)_y = 0,$$
$$(\rho u)_t + (\rho u^2 + p)_x + (\rho uv)_y = 0,$$
$$(\rho v)_t + (\rho uv)_x + (\rho v^2 + p)_y = \rho,$$
$$E_t + [u(E + p)]_x + [v(E + p)]_y = \rho v,$$

and then use the setting from [54, 62] with the following initial conditions:

$$(\rho, u, v, p)(x, y, 0) = \begin{cases} (2, 0, -0.025c \cos(8\pi x), 2y + 1), & y < 0.5, \\ (1, 0, -0.025c \cos(8\pi x), y + 1.5), & \text{otherwise,} \end{cases}$$

where $c := \sqrt{\gamma p / \rho}$ is the speed of sound. The solid wall boundary conditions are imposed at $x = 0$ and $x = 0.25$, and the following Dirichlet boundary conditions are specified at the top and bottom boundaries:

$$(\rho, u, v, p)(x, 1, t) = (1, 0, 0, 2.5), \quad (\rho, u, v, p)(x, 0, t) = (2, 0, 0, 1).$$

We compute the numerical solution until the final time $t = 2.95$ by the limited and adaptive (with $C = 2$) schemes on the computational domain $[0, 0.25] \times [0, 1]$ on the uniform mesh with $\Delta x = \Delta y = 1/800$. The numerical results at $t = 1.95$ and 2.95 are presented in Fig. 21. As we can see, there are pronounced differences between the limited and adaptive solutions. Therefore, one can conclude that the adaptive scheme achieves a much better resolution, which again demonstrates that the adaptive scheme is less dissipative than the limited scheme.

In Fig. 22, we show the regions which the LSI detected as rough at the final time. As one can see, the limited WENO-Z interpolation is only used in a relatively small part of the computational domain.
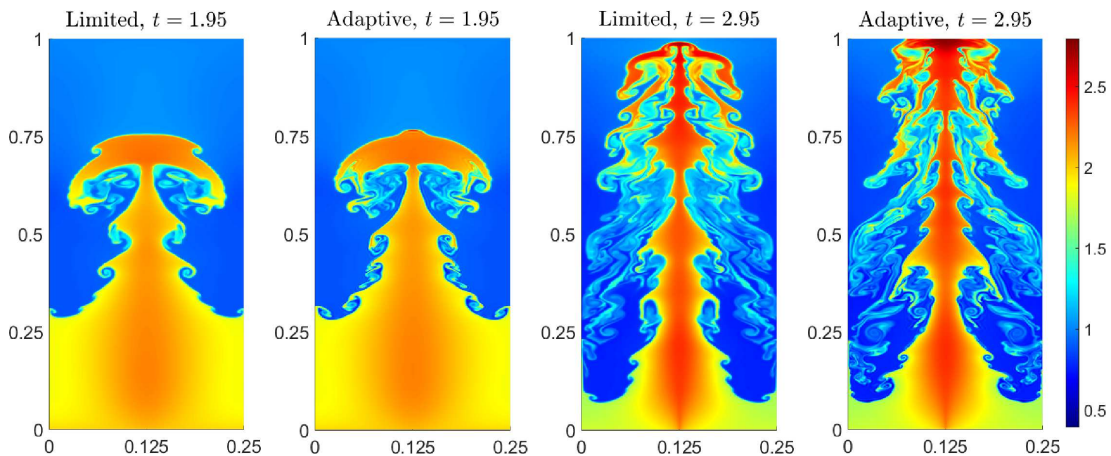

Figure 21: Example 5.11: Density ρ computed by the limited and adaptive schemes at $t = 1.95$ and 2.95.
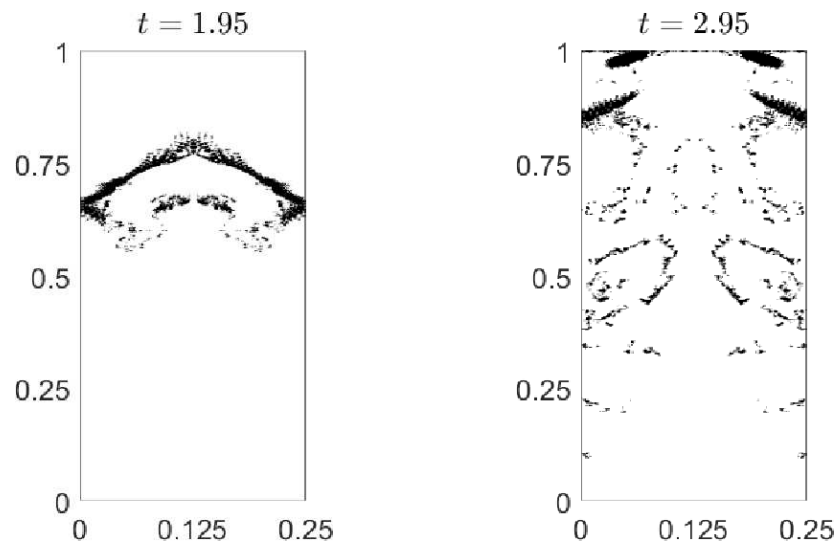
Figure 22: Example 5.11: The limited WENO-Z interpolation is used only in the part of the computational domain indicated by the black color.

As in Example 5.10, we also approximate the dissipative weak solution using the Cesàro averages computed by (5.5) with the same sequence of meshes. We present $\rho^C(1/2^{10})$ computed by the limited and adaptive schemes in Fig. 23 at the times $t = 1.95$ and 2.95. Once again, one can observe that the adaptive scheme better resolves the limiting dissipative weak solution.

Remark 5.3. In this example, the solution is symmetric with respect to the vertical axis $x = 0.125$. In order to enforce this symmetry, we have applied the strategy from [62]:
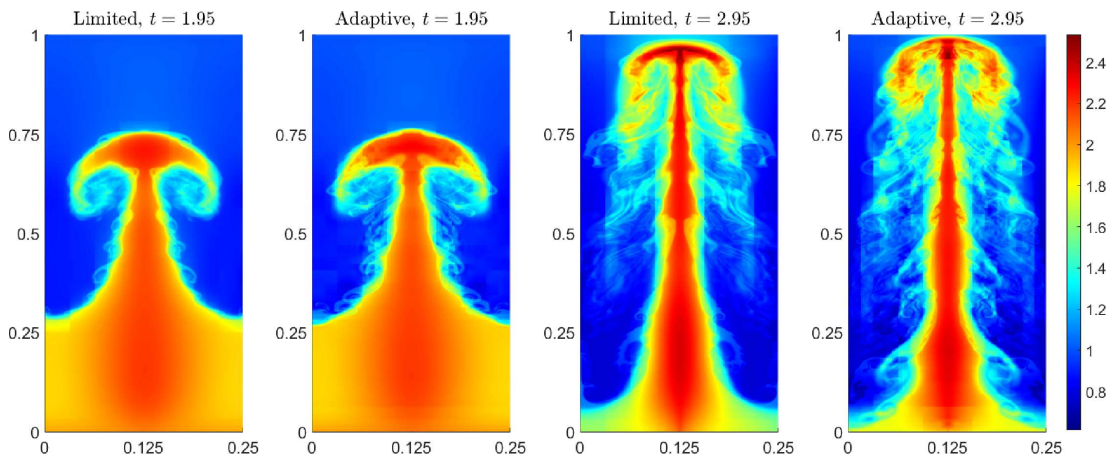

Figure 23: Example 5.11: Cesàro averages of the density $\rho^C(1/2^{10})$ computed by the limited and adaptive schemes at $t = 1.95$ and 2.95.

upon completion of each time evolution step, we replace the computed cell averages $\boldsymbol{U}_{j,k}$ with $\widehat{\boldsymbol{U}}_{j,k}$, where

$$\widehat{\rho}_{j,k} = \frac{\rho_{j,k} + \rho_{M-j,k}}{2}, \quad (\widehat{\rho u})_{j,k} = \frac{(\rho u)_{j,k} - (\rho u)_{M-j,k}}{2},$$

$$\widehat{E}_{j,k} = \frac{E_{j,k} + E_{M-j,k}}{2}, \quad (\widehat{\rho v})_{j,k} = \frac{(\rho v)_{j,k} + (\rho v)_{M-j,k}}{2}$$

for all j, k under the assumption that $j = 1, \dots, M$. Alternative symmetry enforcement techniques can be found in, e.g., [16, 17, 20, 61].

Remark 5.4. As in the 1-D case, we also compare the computational costs of the studied limited and adaptive A-WENO schemes and present the CPU times consumed by the adaptive scheme relative to the fully limited one. The obtained results are presented in Table 5, where one can see that in the 2-D case, the difference in CPU times is slightly smaller than in the 1-D examples, but the adaptive scheme is still clearly more efficient.

Table 5: Examples 5.7-5.11: CPU times consumed by the adaptive A-WENO scheme relative to the fully limited A-WENO scheme.

Example 5.7	Example 5.8	Example 5.9	Example 5.10	Example 5.11
80%	81%	81%	80%	83%

6. Conclusion

In this paper, we have developed new adaptive alternative weighted essentially non-oscillatory (A-WENO) schemes for one- and two-dimensional hyperbolic systems of conservation laws. The proposed schemes employ the scheme adaption strategy, according to which the limited WENO-Z interpolation is only used to capture rough parts of the computed solution, while in the smooth areas, nonlimited fifth-order interpolant is implemented. The rough regions are detected using a smoothness indicator. We have proposed a new, simple and robust local smoothness indicator, which is based on the solutions computed at each of the three stages of the three-stage third-order strong stability preserving Runge-Kutta time integrator. We have applied the new one- and two-dimensional adaptive A-WENO schemes to the Euler equations of gas and dynamics using the recently proposed local characteristic decomposition based central-upwind numerical fluxes. We have conducted several numerical experiments and demonstrated that the new adaptive schemes are essentially non-oscillatory and robust and, at the same time, more accurate than their fully limited counterparts.

In order to illustrate the high efficiency of the proposed adaptive A-WENO schemes, we have compared the CPU times consumed by the studied fully limited and adaptive schemes in each numerical example. From the reported results, we conclude that the introduced

scheme adaption strategy leads to more efficient and, at the same time, more accurate A-WENO schemes. It should also be noted that if the LCD-based CU numerical fluxes implemented in (2.2) and (2.7) are replaced with any other finite-volume (FV) numerical fluxes, the resulting adaptive A-WENO schemes will still be substantially more efficient than the corresponding fully limited A-WENO schemes. However, the difference in the CPU times may vary depending on the computational cost of the particular FV fluxes used.

Appendix A. The 1-D Fifth-Order WENO-Z Interpolant

Here, we briefly describe the fifth-order WENO-Z interpolant.

Assume that the point values W_j of a certain function $W(x)$ at the uniform grid points $x = x_j$ are available. We now show how to obtain an interpolated left-sided value of W at $x = x_{j+1/2}$, denoted by $W_{j+1/2}^-$. The right-sided value $W_{j+1/2}^+$ can then be obtained in the mirror-symmetric way.

The term $W_{j+1/2}^-$ is computed using a weighted average of the three parabolic interpolants $\mathscr{P}_0(x)$, $\mathscr{P}_1(x)$ and $\mathscr{P}_2(x)$ obtained using the stencils $[x_{j-2}, x_{j-1}, x_j]$, $[x_{j-1}, x_j, x_{j+1}]$, and $[x_j, x_{j+1}, x_{j+2}]$, respectively

$$W_{j+1/2}^- = \sum_{k=0}^{2} \omega_k \mathscr{P}_k(x_{j+1/2}), \tag{A.1}$$

where

$$\begin{aligned}
\mathscr{P}_0(x_{j+1/2}) &= \frac{3}{8} W_{j-2} - \frac{5}{4} W_{j-1} + \frac{15}{8} W_j, \\
\mathscr{P}_1(x_{j+1/2}) &= -\frac{1}{8} W_{j-1} + \frac{3}{4} W_j + \frac{3}{8} W_{j+1}, \\
\mathscr{P}_2(x_{j+1/2}) &= \frac{3}{8} W_j + \frac{3}{4} W_{j+1} - \frac{1}{8} W_{j+2}.
\end{aligned} \tag{A.2}$$

Using a straightforward Taylor expansion one can show that (A.1)-(A.2) is fifth-order accurate if one takes the weights ω_k in (A.1) to be

$$\omega_k = \breve{\omega}_k := \frac{d_k}{d_0 + d_1 + d_2}, \quad d_0 = \frac{1}{16}, \quad d_1 = \frac{5}{8}, \quad d_2 = \frac{5}{16}, \tag{A.3}$$

resulting in the nonlimited point values, which we denote by

$$\breve{W}_{j+1/2}^- := \sum_{k=0}^{2} \breve{\omega}_k \mathscr{P}_k(x_{j+1/2}) = \frac{3}{128} W_{j-2} - \frac{5}{32} W_{j-1} + \frac{45}{64} W_j + \frac{15}{32} W_{j+1} - \frac{5}{128} W_{j+2}.$$

The computed interpolation may, however, be oscillatory in rough areas of $W(x)$ and thus the values $\breve{W}_{j+1/2}^-$ need to be modified by replacing the weights (A.3) there with

$$\omega_k = \widetilde{\omega}_k := \frac{\alpha_k}{\alpha_0 + \alpha_1 + \alpha_2}, \quad \alpha_k = d_k \left[1 + \left(\frac{\tau_5}{\beta_k + \varepsilon} \right)^p \right], \quad \tau_5 = |\beta_2 - \beta_0|, \tag{A.4}$$

and thus obtaining the limited WENO-Z point values

$$\widetilde{W}^-_{j+1/2} := \sum_{k=0}^{2} \widetilde{\omega}_k \mathscr{P}_k(x_{j+1/2}). \tag{A.5}$$

In (A.4), β_k are the following smoothness indicators for the corresponding parabolic interpolants $\mathscr{P}_k$:

$$\beta_k = \sum_{\ell=1}^{2} (\Delta x)^{2\ell-1} \int_{C_j} \left(\frac{\partial^\ell \mathscr{P}_k}{\partial x^\ell} \right)^2 dx, \quad k = 0, 1, 2. \tag{A.6}$$

Evaluating the integrals in (A.6), we obtain

$$\beta_0 = \frac{13}{12}\left(W_{j-2} - 2W_{j-1} + W_j\right)^2 + \frac{1}{4}\left(W_{j-2} - 4W_{j-1} + 3W_j\right)^2,$$

$$\beta_1 = \frac{13}{12}\left(W_{j-1} - 2W_j + W_{j+1}\right)^2 + \frac{1}{4}\left(W_{j-1} - W_{j+1}\right)^2, \tag{A.7}$$

$$\beta_2 = \frac{13}{12}\left(W_j - 2W_{j+1} + W_{j+2}\right)^2 + \frac{1}{4}\left(3W_j - 4W_{j+1} + W_{j+2}\right)^2.$$

Finally, in all of the numerical examples reported in this paper, we have used $p = 2$ and $\varepsilon = 10^{-12}$.

Appendix B. 1-D Local Characteristic Decomposition

Even though the WENO-Z interpolant (A.1), (A.4), (A.5), (A.7) is essentially non-oscillatory, it is well-known that its application to the conservative variables U in a componentwise manner may lead to spurious oscillations in the computed solution. We, therefore, implement the reconstruction procedure described in Appendix A in the LCD framework.

Specifically, we first introduce the matrix $\widehat{A}_{j+1/2} := A(\widehat{U}_{j+1/2})$, where $\widehat{U}_{j+1/2}$ is either a simple average $(U_j + U_{j+1})/2$ or another type of average of the U_j and U_{j+1} states (in the numerical examples reported in Sections 3 and 5, we have used the simple average). As long as the system (1.1) is strictly hyperbolic, we compute the matrices $R_{j+1/2}$ and $R^{-1}_{j+1/2}$ such that $R^{-1}_{j+1/2}\widehat{A}_{j+1/2}R_{j+1/2}$ is a diagonal matrix and introduce the local characteristic variables in the neighborhood of $x = x_{j+1/2}$

$$\Gamma_m = R^{-1}_{j+1/2}U_m, \quad m = j-2, \dots, j+3.$$

Equipped with the values Γ_{j-2}, Γ_{j-1}, Γ_j, Γ_{j+1}, Γ_{j+2}, and Γ_{j+3}, we apply the interpolation procedure described in Appendix A to each of the components $\Gamma^{(i)}$, $i = 1, \dots, d$ of Γ and obtain either the nonlimited $\breve{\Gamma}^-_{j+1/2}$ or limited $\widetilde{\Gamma}^-_{j+1/2}$ point values. The values $\breve{\Gamma}^+_{j+1/2}$ and $\widetilde{\Gamma}^+_{j+1/2}$ are computed, as mentioned in Appendix A, in the mirror-symmetric way. Finally, the corresponding nonlimited and limited point values of U are given by

$$\breve{U}^\pm_{j+1/2} = R_{j+1/2}\breve{\Gamma}^\pm_{j+1/2}, \quad \widetilde{U}^\pm_{j+1/2} = R_{j+1/2}\widetilde{\Gamma}^\pm_{j+1/2},$$

respectively.

Remark B.1. A detailed explanation of how the average matrix $\widehat{A}_{j+1/2}$ and the corresponding matrices $R_{j+1/2}$ and $R_{j+1/2}^{-1}$ are computed in the case of the Euler equation of gas dynamics can be found in, e.g., [13].

Acknowledgments

References

[1] R. Abgrall, *On essentially non-oscillatory schemes on unstructured meshes: Analysis and implementation*, J. Comput. Phys. **114**, 45–58 (1994).

[2] N.A. Adams and K. Shariff, *A high-resolution hybrid compact-ENO scheme for shock-turbulence interaction problems*, J. Comput. Phys. **127**, 27–51 (1996).

[3] F. Aràndiga, A. Baeza and R. Donat, *Vector cell-average multiresolution based on Hermite interpolation*, Adv. Comput. Math. **28**, 1–22 (2008).

[4] F. Aràndiga and R. Donat, *Nonlinear multiscale decompositions: The approach of A. Harten*, Numer. Algorithms **23**, 175–216 (2000).

[5] F. Aràndiga, R. Donat and A. Harten, *Multiresolution based on weighted averages of the hat function. II. Nonlinear reconstruction techniques*, SIAM J. Sci. Comput. **20**, 1053–1093 (1999).

[6] D.S. Balsara, S. Garain, V. Florinski and W. Boscheri, *An efficient class of WENO schemes with adaptive order for unstructured meshes*, J. Comput. Phys. **404**, 109062 (2020).

[7] D.S. Balsara, S. Garain and C.-W. Shu, *An efficient class of WENO schemes with adaptive order*, J. Comput. Phys. **326**, 780–804 (2016).

[8] M. Ben-Artzi and J. Falcovitz, *Generalized Riemann problems in computational fluiddynamics*, in: *Cambridge Monographs on Applied and Computational Mathematics, Vol. 11*, Cambridge University Press (2003).

[9] M.J. Berger and P. Colella, *Local adaptive mesh refinement for shock hydrodynamics*, J. Comput. Phys. **82**, 64–84 (1989).

[10] M.J. Berger and J. Oliger, *Adaptive mesh refinement for hyperbolic partial differential equations*, J. Comput. Phys. **53**, 484–512 (1984).

[11] R. Borges, M. Carmona, B. Costa and W.S. Don, *An improved weighted essentially non-oscillatory scheme for hyperbolic conservation laws*, J. Comput. Phys. **227**, 3191–3211 (2008).

[12] M. Castro, B. Costa and W.S. Don, *High order weighted essentially non-oscillatory WENO-Z schemes for hyperbolic conservation laws*, J. Comput. Phys. **230**, 1766–1792 (2011).

[13] A. Chertock, S. Chu, M. Herty, A. Kurganov and M. Lukáčová-Medviďová, *Local characteristic decomposition based central-upwind scheme*, J. Comput. Phys. **473**, 111718 (2023).

[14] B. Costa and W.S. Don, *High order hybrid central-WENO finite difference scheme for conservation laws*, J. Comput. Appl. Math. **204**, 209–218 (2007).

[15] J. Dewar, A. Kurganov and M. Leopold, *Pressure-based adaption indicator for compressible Euler equations*, Numer. Meth. Part. D. E. **31**, 1844–1874 (2015).

[16] W.S. Don, D.-M. Li, Z. Gao and B.-S. Wang, *A characteristic-wise alternative WENO-Z finite*

difference scheme for solving the compressible multicomponent non-reactive flows in the overestimated quasi-conservative form, J. Sci. Comput. **82**, 27 (2020).

[17] W.S. Don, P. Li, K.Y. Wong and Z. Gao, *Improved symmetry property of high order weighted essentially non-oscillatory finite difference schemes for hyperbolic conservation laws*, Adv. Appl. Math. Mech. **10**, 1418–1439 (2018).

[18] E. Feireisl, M. Lukáčová-Medviďová, H. Mizerová and B. She, *Numerical analysis of compressible fluid flows*, in: *MS&A. Modeling, Simulation and Applications, Vol. 20*, Springer (2021).

[19] U.S. Fjordholm, S. Mishra and E. Tadmor, *On the computation of measure-valued solutions*, Acta Numer. **25**, 567–679 (2016).

[20] N. Fleischmann, S. Adami and N.A. Adams, *Numerical symmetry-preserving techniques for low-dissipation shock-capturing schemes*, Comput. & Fluids **189**, 94–107 (2019).

[21] Z. Gao, L.-L. Fang, B.-S. Wang, Y. Wang and W.S. Don, *Seventh and ninth orders alternative WENO finite difference schemes for hyperbolic conservation laws*, Comput. & Fluids **202**, 104519 (2020).

[22] A. Gelb and E. Tadmor, *Adaptive edge detectors for piecewise smooth data based on the minmod limiter*, J. Sci. Comput. **28**, 279–306 (2006).

[23] A. Gelb and E. Tadmor, *Spectral reconstruction of piecewise smooth functions from their discrete data*, M2AN Math. Model. Numer. Anal. **36**, 155–175 (2020).

[24] S. Gottlieb, D. Ketcheson and C.-W. Shu, *Strong Stability Preserving Runge-Kutta and Multistep Time Discretizations*, World Scientific Publishing Co. Pte. Ltd. (2011).

[25] S. Gottlieb, C.- W. Shu and E. Tadmor, *Strong stability-preserving high-order time discretization methods*, SIAM Rev. **43**, 89–112 (2001).

[26] J.-L. Guermond and R. Pasquetti, *Entropy-based nonlinear viscosity for Fourier approximations of conservation laws*, C. R. Math. Acad. Sci. Paris. **346**, 801–806 (2008).

[27] J.-L. Guermond, R. Pasquetti and B. Popov, *Entropy viscosity method for nonlinear conservation laws*, J. Comput. Phys. **230**, 4248–4267 (2011).

[28] A. Harten, B. Engquist, S. Osher and S.R. Chakravarty, *Uniformly high-order accurate essentially nonoscillatory schemes. III*, J. Comput. Phys. **43**, 231–303 (1987).

[29] A. Harten and S. Osher, *Uniformly high-order accurate essentially nonoscillatory schemes. I*, SIAM J. Numer. Anal. **24**, 279–309 (1987).

[30] J.S. Hesthaven, *Numerical Methods for Conservation Laws: From Analysis to Algorithms* in: *Computational Science and Engineering*, SIAM (2018).

[31] G.-S. Jiang and C.-W. Shu, *Efficient implementation of weighted ENO schemes*, J. Comput. Phys. **126**, 202–228 (1996).

[32] Y. Jiang, C.-W. Shu and M.P. Zhang, *An alternative formulation of finite difference weighted ENO schemes with Lax-Wendroff time discretization for conservation laws*, SIAM J. Sci. Comput. **35**, A1137–A1160 (2013).

[33] S. Karni and A. Kurganov, *Local error analysis for approximate solutions of hyperbolic conservation laws*, Adv. Comput. Math. **22**, 79–99 (2005).

[34] S. Karni, A. Kurganov and G. Petrova, *A smoothness indicator for adaptive algorithms for hyperbolic systems*, J. Comput. Phys. **178**, 323–341 (2002).

[35] D.I. Ketcheson, R.J. LeVeque and M.J. del Razo, *Riemann Problems and Jupyter Solutions*, in: *Fundamentals of Algorithms, Vol. 16*, SIAM (2020).

[36] A. Kurganov and Y. Liu, *New adaptive artificial viscosity method for hyperbolic systems of conservation laws*, J. Comput. Phys. **231**, 8114–8132 (2012).

[37] A. Kurganov, M. Prugger and T. Wu, *Second-order fully discrete central-upwind scheme for two-dimensional hyperbolic systems of conservation laws*, SIAM J. Sci. Comput. **39**, A947–A965 (2017).

[38] A. Kurganov and E. Tadmor, *Solution of two-dimensional Riemann problems for gas dynamics without Riemann problem solvers*, Numer. Meth. Part. D. E. **18**, 584–608 (2002).

[39] A. Kurganov and R. Xin, *New low-dissipation central-upwind scheme*, Submitted. Preprint available at `https://sites.google.com/view/alexander-kurganov/publications`.

[40] R.J. LeVeque, *Finite Volume Methods for Hyperbolic Problems*, in: *Cambridge Texts in Applied Mathematics*, Cambridge University Press (2002).

[41] G. Li and J. Qiu, *Hybrid weighted essentially non-oscillatory schemes with different indicators*, J. Comput. Phys. **229**, 8105–8129 (2010).

[42] R. Liska and B. Wendroff, *Comparison of several difference schemes on 1D and 2D test problems for the Euler equations*, SIAM J. Sci. Comput. **25**, 995–1017 (2003).

[43] H. Liu, *A numerical study of the performance of alternative weighted ENO methods based on various numerical fluxes for conservation law*, Appl. Math. Comput. **296**, 182–197 (2017).

[44] X.-D. Liu, S. Osher and T. Chan, *Weighted essentially non-oscillatory schemes*, J. Comput. Phys. **115**, 200–212 (1994).

[45] J. Panuelos, J. Wadsley and N. Kevlahan, *Low shear diffusion central schemes for particle methods*, J. Comput. Phys. **414**, 109454 (2020).

[46] S. Pirozzoli, *Conservative hybrid compact-WENO schemes for shock-turbulence interaction*, J. Comput. Phys. **178**, 81–117 (2002).

[47] K.G. Powell, P.L. Roe and J. Quirk, *Adaptive-Mesh Algorithms for Computational Fluid Dynamics*, in: *Algorithmic Trends in Computational Fluid Dynamics (1991), pp. 303–337, ICASE/NASA LaRC Ser.*, Springer (1993).

[48] G. Puppo, *Numerical entropy production for central schemes*, SIAM J. Sci. Comput. **25**, 1382–1415 (2003/04).

[49] G. Puppo and M. Semplice, *Numerical entropy and adaptivity for finite volume schemes*, Commun. Comput. Phys. **10**, 1132–1160 (2011).

[50] J. Qiu and C.-W. Shu, *A comparison of troubled-cell indicators for Runge-Kutta discontinuous Galerkin methods using weighted essentially nonoscillatory limiters*, SIAM J. Sci. Comput. **27**, 995–1013 (2005).

[51] J.J. Quirk, *A parallel adaptive grid algorithm for computational shock hydrodynamics*, Appl. Numer. Math. **20**, 427–453 (1996).

[52] C.W. Schulz-Rinne, *Classifcation of the Riemann problem for two-dimensional gas dynamics*, SIAM J. Math. Anal. **24**, 76–88 (1993).

[53] C.W. Schulz-Rinne, J.P. Collins and H.M. Glaz, *Numerical solution of the Riemann problem for two-dimensional gas dynamics*, SIAM J. Sci. Comput. **14**, 1394–1414 (1993).

[54] J. Shi, Y.-T. Zhang and C.-W. Shu, *Resolution of high order WENO schemes for complicated fow structures*, J. Comput. Phys. **186**, 690–696 (2003).

[55] C.-W. Shu, *High order weighted essentially nonoscillatory schemes for convection dominated problems*, SIAM Rev. **51**, 82–126 (2009).

[56] C.-W. Shu, *Essentially non-oscillatory and weighted essentially non-oscillatory schemes*, Acta Numer. **5**, 701–762 (2020).

[57] C.-W. Shu and S. Osher, *Efficient implementation of essentially non-oscillatory shock-capturing schemes*, J. Comput. Phys. **77**, 439–471 (1988).

[58] C.-W. Shu and S. Osher, *Efficient implementation of essentially non-oscillatory shock-capturing schemes II*, J. Comput. Phys. **83**, 32–78 (1989).

[59] G.A. Sod, *A survery of several finite difference methods for systems of nonlinear hyperbolic conservation laws*, J. Comput. Phys. **27**, 1–31 (1978).

[60] E.F. Toro, *Riemann Solvers and Numerical Methods for Fluid Dynamics. A Practical Introduction*, Springer-Verlag (2009).

[61] H. Wakimura, S. Takagi and F. Xiao, *Symmetry-preserving enforcement of low-dissipation method based on boundary variation diminishing principle*, Comput. & Fluids **233**, 105227 (2022).

[62] B.-S. Wang, W.S. Don, N.K. Garg and A. Kurganov, *Fifth-order A-WENO finite-difference schemes based on a new adaptive diffusion central numerical flux*, SIAM J. Sci. Comput. **42**, A3932–A3956 (2020).

[63] B.-S. Wang, W.S. Don, A. Kurganov and Y. Liu, *Fifth-order A-WENO schemes based on the adaptive diffusion central-upwind Rankine-Hugoniot fluxes*, Commun. Appl. Math. Comput. (2021).

[64] B.-S. Wang, P. Li, Z. Gao and W.S. Don, *An improved fifth order alternative WENO-Z finite difference scheme for hyperbolic conservation laws*, J. Comput. Phys. **374**, 469–477 (2018).

[65] Y. Zheng, *Systems of Conservation Laws: Two-Dimensional Riemann problems*, in: *Progress in Nonlinear Differential Equations and their Applications*, Birkhäuser (2001).

[66] H. Zhu and J. Qiu, *Adaptive Runge-Kutta discontinuous Galerkin methods using different indicators: One-dimensional case*, J. Comput. Phys. **228**, 6957–6976 (2009).